minerals

MDPI

Article

Influence of P and Ti on Phase Formation at Solidification of Synthetic Slag Containing Li, Zr, La, and Ta

Thomas Schirmer [1,*], Hao Qiu [2], Daniel Goldmann [2], Christin Stallmeister [3] and Bernd Friedrich [3]

[1] Department of Mineralogy, Geochemistry, Salt Deposits, Institute of Disposal Research, Clausthal University of Technology, Adolph-Roemer-Str. 2A, 38678 Clausthal-Zellerfeld, Germany
[2] Department of Mineral and Waste Processing, Institute of Mineral and Waste Processing, Waste Disposal and Geomechanics, Clausthal University of Technology, Walther-Nernst-Str. 9, 38678 Clausthal-Zellerfeld, Germany; hao.qiu@tu-clausthal.de (H.Q.); daniel.goldmann@tu-clausthal.de (D.G.)
[3] Institute of Process Metallurgy and Metal Recycling, RWTH Aachen University, Intzestr. 3, 52056 Aachen, Germany; cstallmeister@ime-aachen.de (C.S.); bfriedrich@ime-aachen.de (B.F.)
* Correspondence: thomas.schirmer@tu-clausthal.de; Tel.: +49-5323-722917

Abstract: In the future, it will become increasingly important to recover critical elements from waste materials. For many of these elements, purely mechanical processing is not efficient enough. An already established method is pyrometallurgical processing, with which many of the technologically important elements, such as Cu or Co, can be recovered in the metal phase. Ignoble elements, such as Li, are known to be found in the slag. Even relatively base or highly redox-sensitive elements, such as Zr, REEs, or Ta, can be expected to accumulate in the slag. In this manuscript, the methods for determining the phase formation and the incorporation of these elements were developed and optimized, and the obtained results are discussed. For this purpose, oxide slags were synthesized with Al, Si, Ca, and the additives, P and Ti. To this synthetic slag were added the elements, Zr and La (which can be considered proxies for the light REEs), as well as Ta. On the basis of the obtained results, it can be concluded that Ti or P can have strong influences on the phase formation. In the presence of Ti, La, and Ta, predominantly scavenged by perovskite ($Ca_{1-w}La_{2/3w}Ti_{1-(x+y+z)}Al_{4/3x}Zr_yTa_{4/5z}O_3$), and Zr predominantly as zirconate ($Ca_{1-w}La_{2/3w}Zr_{4-(x+y+z)}Al_{4/3x}Ti_yTa_{4/5z}O_9$), with the P having no effect on this behavior. Without Ti, the Zr and Ta are incorporated into the pyrochlore ($La_{2-x}Ca_{3/2x-y}Zr_{2+2/4y-z}Ta_{4/5z}O_7$), regardless of the presence of phosphorus. In addition to pyrochlore, La accumulates primarily in britholite-type La oxy- or phosphosilicates. Without P and Ti, similar behavior is observed, except that the britholite-like La silicates do not contain P, and the scavenging of La is less efficient. Lithium, on the other hand, forms its own compounds, such as $LiAlO_2$(Si), $LiAl_5O_8$, eucryptite, and Li silicate. Additionally, in the presence of P, Li_3PO_4 is formed, and the eucryptite incorporates P, which indicates an additional P-rich eutectic melt.

Keywords: lithium; titanium; zirconium; lanthanum; tantalum; engineered artificial minerals (EnAM); melt experiments; PXRD; EPMA

Citation: Schirmer, T.; Qiu, H.; Goldmann, D.; Stallmeister, C.; Friedrich, B. Influence of P and Ti on Phase Formation at Solidification of Synthetic Slag Containing Li, Zr, La, and Ta. *Minerals* **2022**, *12*, 310. https://doi.org/10.3390/min12030310

Academic Editors: George Blankson Abaka-Wood and Xianping Luo

Received: 1 February 2022
Accepted: 24 February 2022
Published: 28 February 2022

1. Introduction

Because of the possibility of processing waste materials from various sources, the pyrometallurgical approach is very interesting for the recycling of complex technology products. However, some of the relevant elements, such as Li or Mn, are lost in the process, as they migrate into slags [1,2].

The same applies to lanthanum, although the oxygen partial pressure must also be taken into account, since cobalt, too, is only scavenged into an alloy (with copper, for example) under strongly reducing conditions, according to Dańczak et al. [3].

However, with the modern methods of processing, these slags should also be recyclable. One of these methods is flotation. If the size of the crystals is not too small, it is

possible to separate the individual mineral phases efficiently with this processing method. In order to produce concentrates with high contents of the critical elements by separating the individual mineral phases, these elements must be enriched in suitable compounds. These requirements are now being addressed with the engineered artificial mineral (EnAM) approach. In this approach, the goal is to find a phase for the required elements that will:

(a) Scavenge the element as quantitatively as possible from the (slag) melt;
(b) Will not be affected by other competing compounds (e.g., early crystallizates);
(c) Best form large isometric crystals or aggregates.

The first step of this approach is to study the behavior of the elements in the slag to find the most promising compounds. In the case of lithium in aluminum-rich slags, for example, this is $LiAlO_2$ [1]. However, the behavior of this element when P is present in addition to Si and Al is unknown.

Compared to lithium-ion batteries with liquid electrolytes, all-solid-state Li batteries have the potential to achieve higher safety and higher energy density [4–6]. Therefore, all-solid-state batteries are considered as a promising development direction for lithium-ion batteries. Solid-state electrolyte materials are the core components of all-solid-state batteries, and they can be classified as oxide, sulfide, and polymer, or as inorganic composite solid-state electrolytes [4–7]. According to their material structures, garnet-like solid-state electrolytes, such as $Li_7La_3Zr_2O_{12}$ (LLZ), and NASICON-type solid-state electrolytes, such as $Li_{1+x}Al_xTi_{2-x}(PO_4)$) (LATP), are considered for this application [6,8–11]. Therefore, in the near future, the recovery of elements such as Ti, Zr, La, and Ta from these electrolyte materials will become an issue. In this context, Schwich et al. propose a combined thermal treatment and hydrometallurgical process for these two representative all-solid-state batteries made of LLZ + NMC and LATP + NMC for the recovery of La, Ta, Zr, and Li [12].

However, there is very little published research on the pyrometallurgical recycling process for all-solid-state batteries. This paper studied the influence of La, Ta, Zr, and Li in the CaO-Al_2O_3-SiO_2 slag system on the formation of the mineral phases. The study is essential for the subsequent slag design using the EnAM strategy, and for establishing a pyrometallurgical recycling process for all-solid-state batteries.

The purpose of the slag design is to enrich the Li, La, Ta, and Zr in specific slag mineral phases. Through an appropriate cooling regime, the target mineral phases crystallize into large crystal sizes, thereby allowing the subsequent separation of the target mineral phases from the gangue mineral phases using beneficiation methods. For instance, when lithium is enriched in the $LiAlO_2$ phase, it can be enriched by flotation [13,14]. In the cases of the perovskite and phosphate mineral phases, corresponding mineral processing approaches also exist [15–17].

The investigations of Elwert et al. [18] reveal that the REEs in slag accumulate in britholite. This indicates a strong affinity of the rare earths (e.g., La) for P.

Additionally, the information on the behavior of the elements, Zr and Ta, in synthetic slag is scarce. To verify the observations already made, and whether other elements affect the affinities, such as Ti or P, which potentially form La-, Zr/Ta-, or even Li-enriching compounds, synthetic slags were prepared and investigated in this research.

To study the interaction of all the elements in the (synthetic) slag, the oxides, Al_2O_3, SiO_2, and CaO were selected as the basic system, since they represent the main part of the typical slag systems of pyrometallurgical processing. To these slags were added the additives, P and Ti, and the elements, Li, Zr, La, and Ta, on the basis of the possible future all-solid-state-battery composition presented by Schwich et al. [12].

To minimize the amorphization and/or cryptocrystalline morphology, appropriately long cooling curves of 60 °C/h to 900 °C, and afterwards, 130 °C/h to room temperature, were applied.

To assess the influence of the additives of these synthetic slags, three samples were selected: one with Ti and P; one with P only; and one without P and Ti.

The selected synthetic slags were analyzed for the bulk chemical compositions with inductively coupled optical emission spectroscopy (ICP-OES), for the bulk mineralogical

composition with powder X-ray diffraction (PXRD), and for the compositions of single crystallites and grains with electron probe microanalysis (EPMA).

2. Background

In the investigated synthetic slags (SyS), the focus is on a rather large number of interesting elements, namely, Li, Ti, Zr, La, and Ta, in an oxide slag matrix containing Al, Si, and Ca. All these elements can interact and form oxide compounds. In this sense, the discussion of all the potential phase systems is beyond the scope of this article. Therefore, a subselection of the systems of particular importance for the phase reactions at the solidification of the SyS will be presented.

2.1. Phase Systems of Li Silicates, Aluminates, and Phosphates

Relevant for this study are the phase systems describing:

(a) $LiAlO_2$(Si) (LiAl), with max. 10 wt.% Si;
(b) Spinel (Sp, $LiAl_5O_8$);
(c) Li silicate ($Li_2Al_2SiO_6$);
(d) Eucryptite-like aluminosilicate (Ec, $LiAlSiO_4$) or (EcP, $Li_{1+x}Al_{1-4/3y}Si_{1-z+y-1/4x}P_{4/5z}O_4$), with max. 5 wt.% P;
(e) Li_3PO_4(Si) (LiP).

Because of Konar et al. [19] and Aoyama et al. [20], the system, Al_2O_3-Li_2O, comprises several stable lithium aluminate compounds, such as: Li_5AlO_4, $LiAlO_2$, and $LiAl_5O_8$. A high-temperature compound, $LiAl_{11}O_{17}$, at 0.8 < Al_2O_3 < 0.92 and > 2200 °C, is mentioned by Konar et al. [19].

$LiAlO_2$ and $LiAl_5O_8$ occur in varying crystal modifications. $LiAlO_2$ can be tetragonal (γ-phase at high temperature) and cubic (α-phase at low temperature). At high temperatures, the $LiAl_5O_8$ forms a cubic spinel, and, at low temperatures, it takes a primitive cubic form [19,21].

SiO_2 and Li_2O can react to the binary phases, Li_8SiO_6, Li_4SiO_4, $Li_6Si_2O_7$, Li_2SiO_3, and $Li_2Si_2O_5$ [22]. At the compositions, Li_4SiO_4 and Li_2SiO_3, there are two thermal barriers.

In the system, Li_2O-SiO_2-Al_2O_3, $LiAlO_2$, $LiAl_5O_8$ (spinel), eucryptite ($LiAlSiO_4$), and spodumene ($LiAlSi_2O_6$), and their crystallization areas, are important for the evaluation of the solidification of Li slag. In the presence of Si, a small amount of aluminum in $LiAlO_2$ can be exchanged by it [23]. This behavior of $LiAlO_2$ was also observed by Schirmer et al. [24].

Eucryptite can be described via the substitution of $Li^+ + Al^{3+} = Si^{4+} + v$ (vacant position) in quartz [23]. The crystal system is trigonal (similar to quartz), with a disordered low temperature α-polymorph, and an ordered β-polymorph. The structure of β-eucryptite is described in detail by Sartbaeva et al. [25]. Interestingly, it is mentioned there that only half of the possible lattice positions for lithium are occupied, so that there is flexibility for the charge compensation and the excess Li. The incorporation of phosphorus via the coupled substitution of $Al^{3+} + P^{5+} \leftrightarrow 2Si^{4+}$ is described by Perrotta and Savage [26].

At normal pressure, spodumene occurs as a monoclinic α and a high-temperature tetragonal β-polymorph, with a transition point at 882 °C. The melting point is at 1606.5 °C ([23] and references therein).

The compound, $Li_2Al_2SiO_6$, seems to be unusual, since it is hardly mentioned in the literature (with the exception of [27]).

For the system, Li_2O—P_2O_5, the compounds, Li_3PO_4, $Li_4P_2O_7$, $Li_5P_3O_{10}$, and $LiPO_3$ are described by Jin et al. in [28] and in the references therein. The reported melting points vary between 652 and 658 (°C) for $LiPO_3$, between 1206 and 1225 (°C) for Li_3PO_4, and between 876 and 885 (°C) for $Li_4P_2O_7$. An estimation of the melting temperature of $Li_5P_3O_{10}$ is at 670 (°C). Li_3PO_4 occurs in an orthorhombic high-temperature α modification [29], and two other orthorhombic modifications (β, γ) [30]. The transition point of α to β is at 1167 °C [29]. $Li_4P_2O_7$ forms trigonal and pseudomonoclinic polymorphs [31], and it has a transition point that was determined to be between 630 and 650 (°C) by Jin et al. [28]. $LiPO_3$ crystallizes in the monoclinic crystal system [32]. $Li_5P_3O_{10}$ could not be synthesized

in a water-free variety. A compound with the formula, $Li_5P_3O_{10}{\cdot}5H_2O$, is reported by Jin et al. [28].

2.2. Phase Systems of Ti, Zr, La, and Ta Oxides

Relevant for this study are the phase systems describing:

(a) A perovskite solid solution (Pv, (Ca,La)(Ti,Al,Ta,Zr)O_3), with La and Ta and traces of Zr;
(b) A zirconate solid solution (ZrC, (Ca,La)(Zr,Ti,Ta)$_4O_9$), with minor/trace amounts of La and Ta;
(c) A pyrochlore solid solution (PyC, (La(Ca))$_2$(Zr(Ta))$_2O_7$), with Ta and minor/trace amounts of Ca.

The base compound, perovskite ($CaTiO_3$), is part of the system, CaO—TiO_2, and it crystallizes in orthorhombic (low-temperature), tetragonal (medium-temperature), and cubic (high-temperature) symmetries. The transition points of the different polymorphs have been published by various authors (e.g., [33–42]). The reported melting point of pure $CaTiO_3$ varies between 1964 and 1970 (°C) [43,44]. The coordination numbers are 6 (Ti/O-octahedron) and 12 (La/O-cuboctahedron) [45]. The ternary system, CaO-TiO_2-La_2O_3, has not yet been mentioned in the investigated literature.

The complete solid solutions of $CaTiO_3$ and $La_{0.67}TiO_3$ were studied by Zhang et al. in [41]. They observed that the crystal symmetry depends on the temperature and the amount of La. At high temperatures (>1500 K), and without La to >500 K, and with pure $La_{0.67}TiO_3$, there exists a temperature conode (boundary line), above which a high-temperature cubic m3m structure (below ~0.85 fraction of $La_{067}TiO_3$) coexists with a high-to-medium-temperature tetragonal 4/mmm structure (above ~0.85 fraction of $La_{0.67}TiO_3$). At lower temperatures (< 1500 °C), and without $La_{0.67}TiO_3$ to room temperature, and a ~0.57 fraction of $La_{0.67}TiO_3$, there exists an area with an orthorhombic Pbnm symmetry. Between the 0.57 and ~0.63 fraction of $La_{0.67}TiO_3$, in a limited low-temperature range (room temp. to ~700 K), the symmetry is orthorhombic (Ibmm). In between these areas, at medium temperatures and up to a $La_{0.67}TiO_3$ fraction of ~0.85, the symmetry is tetragonal (I4/mcm).

Tantalum is known to be incorporated into natural perovskites, such as loparite (Lanth, Na, Sr, Ca)(Ti, Nb, Ta, Fe^{3+})O_3 (e.g., [46]). The same is reported for Zr in natural perovskites in kimberlite, as is reported by Chakhmouradian and Mitchell [47].

The base compound, zirconate (in this case, $CaZr_4O_9$), is part of the system, CaO—ZrO_2. This phase crystallizes in the monoclinic C2/c symmetry [48], and it seems to be unstable and it acts as a precursor to $Ca_6Zr_{19}O_{44}$ [49,50]. The coordination numbers are 8 (Ca/O), and 6, 7, and 8 (Zr/O). The incorporation of minor or trace elements, such as La or Ta, has not yet been reported.

The base compound, pyrochlore (in this case, $La_2Zr_2O_7$), is part of the system, ZrO_2—La_2O_3. This compound is stable to approx. 2300 °C, and it crystallizes in the cubic pyrochlore [51] or the fluorite structure (transition between 1000 and 1450 °C) [52]. The coordination numbers, as reported by Ushakov et al. [53], are 6 (Zr/O-octahedron) and 12 (La/O-cuboctahedron). The coupled substitution of Ta and Ca in $La_2Zr_2O_7$ has not yet been documented. The possibility of the coupled substitution of an earth alkaline ion with a low charge (+2) with a highly charged heavy element ion, such as U (+6), in the pyrochlore, $La_2Zr_2O_7$, is discussed by Tang et al. [54].

The incorporation of Li into perovskite, zirconate, and pyrochlore, or the formation of complex oxides with Li, Ca, Ti, Zr, and La, are plausible because all of the elements except for Ca can form Li compounds (titanate, zirconate, lanthanate). Garnets of the type of $Li_xLa_3Zr_yTa_zO_{12}$ are used as the solid-state electrolyte ($Li_{6.4}La_3Zr_{1.4}Ta_{0.6}O_{12}$, e.g., [55]). The same applies to perovskite ($CaTiO_3$)-based compounds, such as $Li_xLa_yTiO_3$, as is reported by Li et al. ($Li_{0.33}La_{0.557}TiO_3$, [56]).

2.3. Phase Systems of Phosphosilicates

Relevant for this study are the phase systems describing:

(a) Oxysilicate (OxS, $(Ca,La)_2(Si,P)O_5$) with Ca and P;
(b) Britholite-like phosphosilicate (BphS): $Ca_2(Ca,La)_2(Si,Al,P)_3O_{11}$.

The base compound, La_2SiO_5, is part of the system, SiO_2—La_2O_3, with the compounds, $La_2Si_2O_7$, La_2SiO_5, and $La_4Si_3O_{12}$ [57]. The compound, La_2SiO_5, has a $P2_1/c$ monoclinic crystal structure [58]. In this structure, two La sites, with 9-fold coordination to oxygen forming a tricapped trigonal-prismatic polyhedron, and with 7-fold coordination to oxygen, forming a capped octahedral structure, are reported by Fukuda and Iwata [58]. For the system, SiO_2—P_2O_5—La_2O_3, the investigations by El Ouenzerfi [59] prove the existence of lanthanoid-rich apatitic phosphosilicates with comparably low Ca contents. Because of the similar ionic radii, it is plausible that a substitution of Ca^{2+}: La^{3+} = 1: 0.67 and Si^{4+}: P^{5+} = 1: 0.8 can occur (e.g., [60]). This is also plausible for a coupled substitution of $La^{3+} \rightarrow Ca^{2+}/Si^{4+} \rightarrow P^{5+}$ in La_2SiO_5.

Britholite is a naturally occurring phosphosilicate that contains Ca, lanthanoides, and Y, OH-, and F, with a P63 or P63/m hexagonal crystal structure, with a formula similar to $Ca_{5-x}Ce_x[(Si,P)O_4]_3F$ (e.g., [61–63]). Britholite can be derived from the apatite structure by the coupled substitution of $Ca^{2+} \rightarrow La^{3+}/P^{5+} \rightarrow Si^{4+}$ [64,65]. In this structure, one Lanth-position refers to the Ca position in apatite with 9-fold coordination to oxygen. A second Lanth-position is 7-fold coordinated to oxygen, and it forms an irregular capped octahedron that is somewhat similar to those reported for La_2SiO_5.

2.4. Incorporation of Li, Ti, Zr, La, and Ta into Slag

In slag and slag-like material, Li can be present as eucryptite and spodumene [66], or if the slag is Al-dominated, as in $LiAlO_2$ [1]. The occurrence of Li_3PO_4 is documented by Yamauchi and Maruhashi [67].

In a slag that consists only of Al, Ti, and Al, with traces of Mg, Si, and Ca, titanium can occur as Ti_3O_5 and Ti_2O_3 [68]. In high-Ti sorel-slag, armalcolite ($MgO{\cdot}4TiO_2{\cdot}FeO$) can be the main compound [69]. In the presence of Ca, $CaTiO_3$ is one of the main Ti-bearing phases, as is reported by Wang et al. [70]. The mineralogy of Zr and Ta in slag is not discussed much in the literature, although some articles about the leaching or the pyrometallurgical treatment are available. The pseudostructures that describe the next neighbors of the elements in tin slags are described by Gaballah and Allain [71]. The association of Nb, La, Ta, and U to Ca may be an indication of pyrochlore ($(Ca,Na)_2(Ta,Nb)_2O_6(O,Oh,F)$) formation. Additionally, Gaballah and Allain [71] report a relation of Ti and Ca to Ta (and Nb), and this could be an indication of a perovskite structure in some of the investigated slags.

Britholite, or britholite-like phosphosilicates (BphS), are the typical constituents in slag containing REEs. The affinity of Nd and Dy to this compound is documented by Elwert et al. [18]. The occurrence of fluoro-britholite ($Ca_3Ce_2[(Si,P)O_4]_3F$) in slag is what motivated Li et al. [72] to develop the separation method via super gravity and centrifugal casting. The slag surrogates investigated by Stefanovsky et al. [73] describe britholite as the typical phase after solidification, and they assessed its potential for the incorporation of actinides, using Sm as a chemical analogue. Fluoro-britholite ($Ca_9Nd_{1-x}An^{IV}{}_x(PO_4)_{5-x}(SiO_4)_{1-x}F_2$) that contains phosphate ceramics are the topic of the work carried out by Terra et al. [74]. Here, too, the potential of this compound for the immobilization of actinides was investigated.

3. Materials and Methods

3.1. Materials

Chemicals

To produce the SyS, the following raw materials were used in powder form:

(a) Al_2O_3: Alfa Aesar, α-phase, 99.9% (metal basis);
(b) Li_2CO_3: Alfa Aesar, 99%, powder;

(c) La_2O_3: Alfa Aesar, REacton, 99.9% (REO), powder;
(d) ZrO_2: Alfa Aesar, calcined, 99%;
(e) $Ca_3(PO_4)_2$: Acros Organics, 96%, pure, mixture of Calcium phosphates;
(f) Ta_2O_5: Alfa Aesar, 99% (metal basis);
(g) SiO_2: Heraeus Quarzglas GmbH & Co. KG, >99.99%;
(h) TiO_2: KRONOS 3025, ≥99%;
(i) CaO: Carl Roth, ≥96%.

Li_2CO_3 was chosen instead of Li_2O for availability reasons. The carbonate decomposes during the heating process with the release of CO_2, and it thereby forms Li_2O [75]. P_2O_5 is substituted by $Ca_3(PO_4)_2$ because of the acidic and corrosive behavior of P_2O_5 [18].

3.2. Methods

3.2.1. Thermochemical Modeling and Experiments

On the basis of the cell chemistries, "Cell 1.1" and "Cell 2.1", which are presented by Schwich et al. [12], different slag systems were investigated. The liquidus temperature of the possible slag systems that result from the slag-forming oxides that are contained in ASSB (presented in Table 1) and the additional fluxes were thermochemically modeled with FactSage™ 8.0 [75]. For the calculations, the FToxide and FactPS databases in the "Equilib-module" were used [75]. The FToxide database, which is intended for slags, glasses, ceramics, and refractories, contains oxides and oxidic solutions, while the FactPS database was used for the pure substances (solids and gases), except for the duplicates with the FToxide database. The pressure was set at 1 atm, and the equilibrium was calculated. Because of the limited data for the contained REEs, La and Ta, they could not be considered in the model. The additional Al_2O_3, as well as SiO_2, CaO, and P_2O_5, were considered as the common fluxing components. Their influences on the liquidus temperature of the slags were studied for the different amounts of those oxide additions. The process temperature of the melting tests is 1500 °C. Accordingly, the liquidus temperature of the material mixture must be lower. Without the addition of the fluxing components to the mixture of the slag-forming oxides from the possible battery compositions, the slag would be too high-melting (see Section 4.1).

Table 1. Considered slag-forming oxides from possible battery cell compositions based on Schwich et al. [12].

wt.%	Cell 1.1	Cell 2.1
Al_2O_3	5.7	7.6
Li_2CO_3	33.6	33.6
La_2O_3	18.8	3.5
ZrO_2	8.1	1.4
Ta_2O_5	3.7	0.6
MnO_2	0	0
P_2O_5	0	9.2
TiO_2	0	5.0

The experiments were carried out in a resistance-heated muffle furnace (Nabertherm HT 16/18) with a chamber volume of 160 l. Dense sintered alumina crucibles (C799), with volumes of 150 mL, were filled with the powder mixtures. All of the experiments were carried out under an argon atmosphere, with a constant flow of 12 l/min. The material was heated to 1500 °C with 300 °C/h. For the homogenization, a holding time of 1.5 h at 1500 °C was carried out before the controlled linear cooling with 60 °C/h to 900 °C. From 900 °C to room temperature, a linear cooling rate of 130 °C/h was chosen. To investigate the influence of Ti and P, three SyS compositions were selected, as is described in Section 4.1. One sample contains all of the considered elements; one is without Ti; and one is without Ti and P.

3.2.2. Chemical Bulk Analysis

After the finalization of the experiment, the solid samples were digested using two methods. The samples were digested with a mixture of nitric acid, hydrochloric acid, and hydrofluoric acid in the TurboWAVE digestion autoclave from MLS. In addition, lithium tetraborate was added to the samples and was melted in a platinum crucible at 1050 °C for 20 min, which was followed by leaching with dilute hydrochloric acid. The measurements of the two digestion solutions for the elemental content determination were carried out with ICP-OES (ICP-OES 5100, Agilent, Agilent Technologies Germany GmbH & Co. KG, Waldbronn, Germany).

3.2.3. Mineralogical Investigation

To provide an overview of the mineralogical composition, powder X-ray diffraction (PXRD), using a PANalytical X-Pert Pro diffractometer, which was equipped with a Co X-ray tube (Malvern PANalytical GmbH, Kassel, Germany), was used. The identification was carried out with the pdf-2 ICCD XRD database, with the *American Mineralogist* crystal structure database [76], and with the RRUFF-Structure database [77].

A spatially resolved point analysis, with line scans of the crystals and grains, was carried out with electron probe microanalysis (EPMA). This well-known standard method delivers the chemical data of single spots or line scans via wavelength-dispersive or energy-dispersive X-ray spectroscopy (WDX or EDX), and it delivers the visualization data via electron micrographs with secondary electrons (topography, SE), or backscattered electrons (topography (T), or atomic number (Z) contrast (BSE(T)/BSE(Z)). The measurements were carried out with a Cameca SX FIVE FE (field emission) electron probe, which was equipped with a Schottky electron emitter, SE and BSE detectors, and five wavelength-dispersive (WDX) spectrometers (CAMECA SAS, Gennevilliers Cedex, France). The points were analyzed for the following elements/(lines): Na/Kα, Mg/Kα, Al/Kα, Si/Kα, P/Kα, Ca/Kα, Ti/Kα, Zn/Kα, ZrLα, LaLα, and TaLα, by using an appropriate suite of analyzing crystals. Reference materials provided by P&H Developments Ltd. (Glossop, Derbyshire, UK) and Astimex Standards Ltd. (Toronto, ON, Canada) were used to calibrate the system. The beam size setting was on 0 (zero), which enabled a diameter of substantially below 1 µm (beam diameter of a Schottky-type; see, e.g., Jercinovic et al. [78]). The matrix correction was carried out with the X-PHI model [79].

Lithium is one of the important elements in this study, and it cannot be analyzed using X-ray spectroscopy with sufficient precision because of the rather long wavelength of LiKα, which is accompanied by an extremely low fluorescence yield. Because the chemistry of the samples is well known and contains no refractory light elements, such as Be or B, or other volatile compounds, such as OH^-, H_2O, CO_2, $NO_3{}^-$, Cl^-, or F^-, the Li can be calculated via virtual compounds using the measured elements, as was carried out in [24]. Because of the complex chemistry for the matrix, the Li was calculated as a balance compound in this case. To calculate the Li in LiP and in Li aluminosilicates, single compounds were used (LiP and Li aluminosilicates). The Li in the EcP was calculated in two steps. First, a stoichiometric calculation was performed, which started with Li = Al = Si = 1, and a synchronization with the measurement results (wt.% Al, Si, P) to determine the Li_{tot}. In a second step, the Li value (Li_{vc}) of the pure $LiAlSiO_4$ proportion was calculated using the virtual components, SiO_2 and $LiAlO_2$. The excess Li is the difference: Li_{tot}—Li_{vc}. The calculated Li concentration was then included into an EPMA matrix back-correction (one iteration cycle).

Since these are not measured values, no standard deviations are given for Li* and O*.

The results of the reference measurements and the calculations of the lithium and oxygen are listed in Table 2.

Table 2. Measured and calculated values for spodumene (international reference: Astimex) and pure $LiAlO_2$ (in-house reference). * calculated values.

Spodumene, wt.%	Average (n = 5)	RelStDev	Reference	Recovery (%)
Al	14.5	0.3	14.4	100.4
Si	30.8	0.6	30.0	102.8
Li *	3.73	n.a.	3.71	100.5
O *	52.3	n.a.	51.6	101.4
$LiAlO_2$, wt.%	Average (n = 6)	RelStDev	Reference	Recovery (%)
Al	40.3	0.2	40.9	98.4
Li *	10.4	n.a.	10.5	98.5
O *	47.8	n.a.	48.5	98.5

4. Results

In this section, the measurement results are presented. The section on the mineralogical characterization first describes the morphologies of the three slags. Then, the individual phases that were analyzed in the slags are presented. This is followed by a balance with the calculated semiquantitative phase contents, and the distribution of the elements among these phases.

4.1. Result of Thermochemical Modeling and Chosen Slag Systems

On the basis of Table 1, the FactSage™ [75] calculations were carried out with regard to the melting points of the possible mixtures of the battery oxides with slag-forming elements. In the case of Cell 2.1, the influence of SiO_2 and the additional Al_2O_3 to the battery oxides on the melting point was investigated. Figure 1a shows a decreasing liquidus temperature with the addition of SiO_2. In the case of no additional Al_2O_3, the liquidus temperature decreases from 1837 to 1523 °C with a 12.5 g SiO_2 addition per 100 g of battery material. Since the influence of Al_2O_3 is comparatively low in the desired temperature range, and the Al_2O_3 addition increases the amount of slag, which leads to a dilution of the valuable components, the addition is rejected as a slag additive. The process temperature was set at 1500 °C, so the slag system must have a lower liquidus temperature while minimizing the slag addition quantity. Moreover, the slag should not be too acidic, as glassy solidification is to be avoided for the described investigations. Therefore, the slag system with an addition of 20 g/100 g of battery material and no additional Al_2O_3 was chosen (ASSB-1). The calculated liquidus temperature of this system is 1439 °C. It should be noted that the La_2O_3 and Ta_2O_5 could not be considered in the model and, thus, their influence remains unknown.

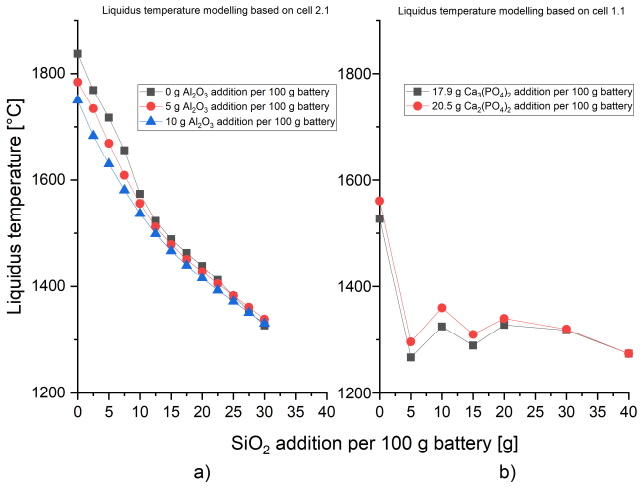

Figure 1. Liquidus temperatures modeled with FactSage™ 8.0 [75] for (**a**) Cell 2.1, and (**b**) Cell 1.1, which are related to the SiO_2 addition.

As the influences of P and Ti on the slag mineralogy were to be investigated, two slag systems were chosen on the basis of the composition of Cell 1.1. Similar to Cell 2.1, the relation between the liquidus temperature and the SiO_2 addition was modeled. Because the system does not contain P, different amounts of $Ca_3(PO4)_2$ were investigated as well. On the basis of Elwert et al. [18], the relation of the REE:PO_4^{3-} was set to 1:1. In addition, a higher P content was examined. As is shown in Figure 1b, a larger amount of $Ca_3(PO_4)_2$ does not have a huge influence on the liquidus temperature and, therefore, the over-stoichiometric P addition was chosen for the trials. The SiO_2 addition was set to 20 g/100 g of the battery material (ASSB-7), which leads to a modeled liquidus temperature of 1340 °C. Smaller addition rates would suffice to decrease the liquidus temperature to 1500 °C, but a deviation that is due to the comparatively high La content, which is not contained in the model, is expected. To investigate the influence of P, System Cell 2.1, with an addition of 30 g of SiO_2 and 11 g of CaO per 100 g of battery material, was chosen (ASSB-10) as the P-free reference. A larger amount of SiO_2 than in ASSB-7 was selected as the replacement for the P_2O_5 and the similar basicity of the slag.

4.2. Bulk Chemistry of the Melt Experiments

Three interesting SyS resulted from the set of experiments that were conducted via the approach described in Section 4.1: one with P and Ti; one with P; and one without P and Ti (Table 3).

Table 3. Chemical bulk compositions of three SyS samples.

wt.%	ASSB-1	ASSB-7	ASSB-10
Al	17.2	11.9	16.4
Ca	6.8	6.6	8.0
La	2.7	13.9	12.3
Li	5.6	5.1	4.6
P	3.3	3.3	-
Si	11.4	8.9	10.3
Ta	0.4	2.6	2.3
Ti	2.8	-	-
Zr	0.9	4.6	4.2

All of the SyS samples contain the slag builders, Al, Ca, and Si, and the possibly recyclable elements, Li, Zr, La, and Ta.

4.3. Comparison of the Compounds in Three SyS

When considering the three selected slags, it should be noted that Sample ASSB-1 has significantly lower contents of Zr, La, and Ta. The reason for these concentration differences is that the samples are from a set of melt experiments that were not prepared solely for the purpose of phase analysis. Unfortunately, this affects the comparability of the observed phase reactions. In the following sections, the results are presented with reference to the individual compounds that were observed. The concentration differences of the important elements in the samples were taken into account as much as possible.

4.3.1. Morphology

The overall morphology of the SyS can be documented by BSE(Z) micrographs, and they show a positive correlation between the average atomic number and the brightness. However, this also means that compounds such as Sp, LiAl, and Ec, with similar average atomic numbers, are very difficult to distinguish via the grey shade. In this case, the morphology may be the only criterion that separates the phases. The overview in Figure 2 shows, for ASSB-1, a dense fine-grained network of skeleton-shaped LiAl, with few idiomorphic spinel grains and heavy element phases. The proportion of bright heavy element phases seems to be rather low (which is due to the distinctively lower bulk heavy element concentrations). The SyS ASSB-7 and ASSB-10 are similar in the respect that there are no

spinel grains, and the grain size of LiAl is distinctively larger than in ASSB-1, but it shows a similar skeleton habitus. Because of the similar bulk concentrations of the heavy elements, the proportions of the bright heavy element phases are similar in ASSB-7 and ASSB-10, and, in both samples, they are higher than in ASSB-1. It is clear from the BSE micrographs that spinel, OxS/BphS, and PyC are the early crystallizates (Figure 2).

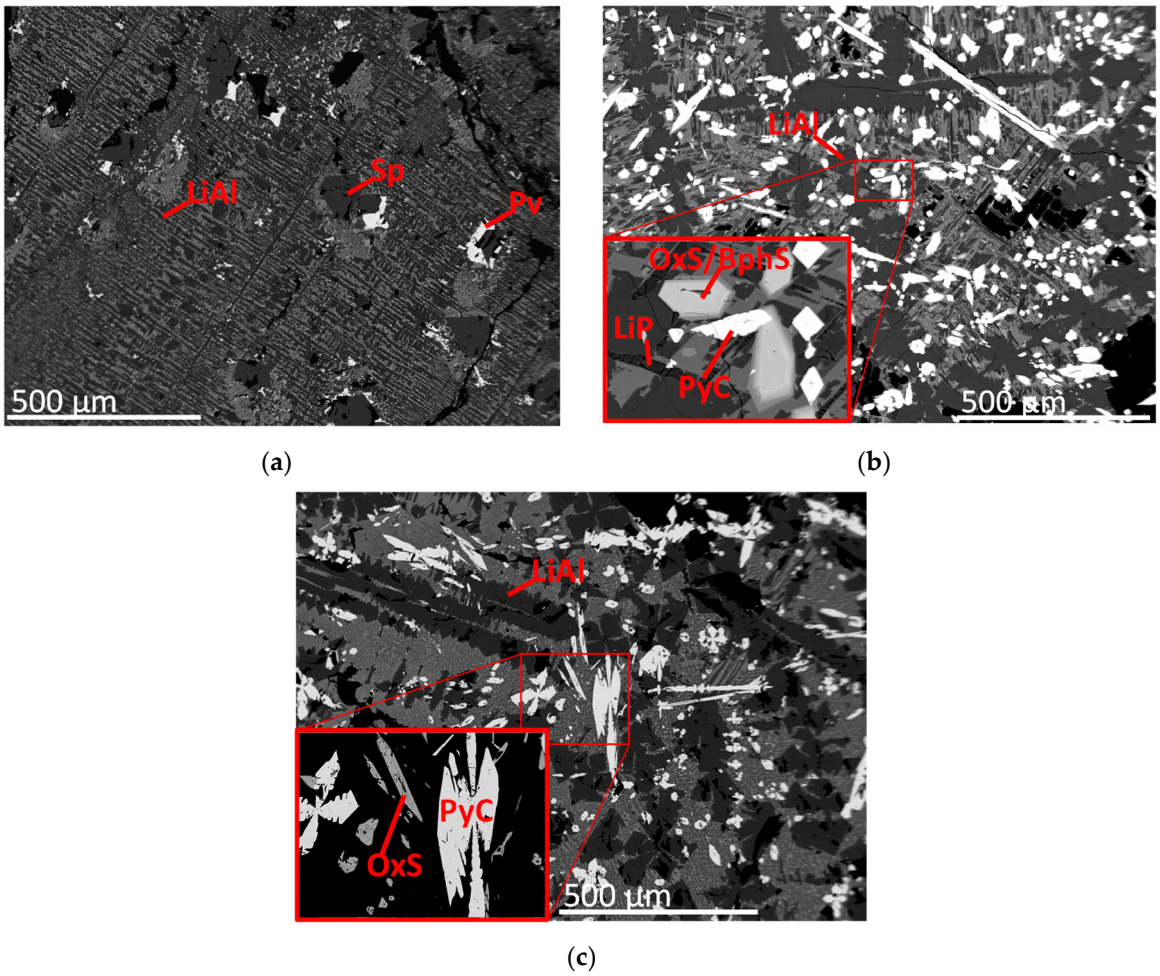

Figure 2. Overview of the morphologies and phase distributions of the three slag samples: ASSB-1 (**a**); ASSB-7 (**b**); and ASSB-10 (**c**), recorded using BSE(Z).

4.3.2. Lithium Aluminate (LiAl)

The PXRD of the LiAl was evaluated using the pdf-2 pattern: 01-073-1338. All three samples contain this compound. There is a tendency that the sample, ASSB-1 (P, Ti), contains the highest amount of LiAl, followed by ASSB-10 (P- and Ti-free) and ASSB-7 (only P). The EPMA single-point measurements show that the LiAl is not pure $LiAlO_2$, but that it incorporates Si (up to ~10 wt.%, Appendix A, Table A1). This behavior is already documented by Schirmer et al. [24]. Throughout the three SyS samples, the chemistries of this compound are quite comparable, but the morphologies are slightly different (Figure 2). The Ti-containing ASSB-1 shows the fine-grained skeleton growth of LiAl (thickness: ~15–20 µm), whereas the skeleton-shaped LiAl grains in ASSB-7 and ASSB-10 can be substantially larger (thickness: ~50–60 µm). Additionally, the LiAl grains in ASSB-7 and ASSB-10 are more of a partly isometric and hypidiomorphic shape. In ASSB-10, in addition to the massive skeleton-shaped LiAl crystals in the matrix, a second generation of small µm-sized skeleton-shaped or single LiAl grains exists.

4.3.3. Spinel (Sp)

To evaluate the PXRD results with respect to the Sp, the pdf-2 pattern, 00-038-1425, was selected. Only ASSB-1 (P, Ti) contains this compound (Figure 3). Moreover, with the EPMA, this phase could only be determined in ASSB-1. This phase contains impurities, such as Zn and Mg, and a small amount of Ti (Appendix A, Table A2). The spinel is characterized by large isometric and idiomorphic grains/crystals (size: ~150–300 µm; Figure 2, upper left).

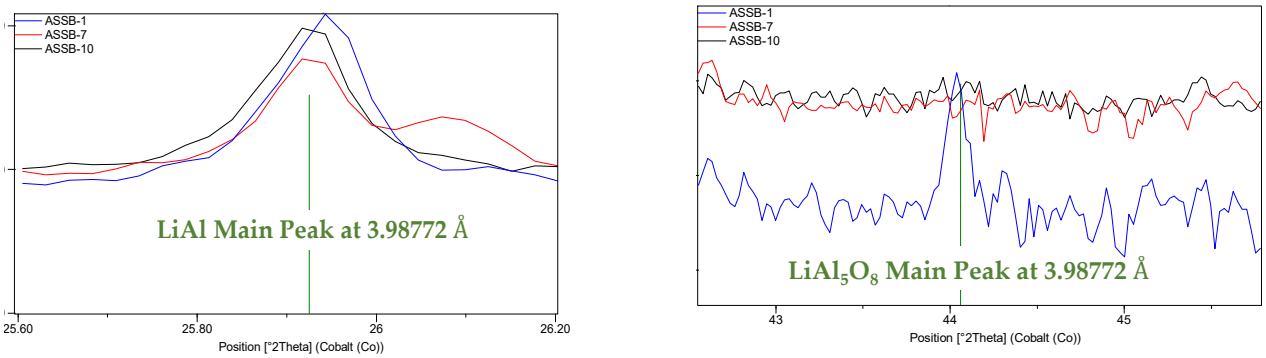

Figure 3. Section of PXRD measurements with the main peaks of LiAl (**left**) and Sp (**right**).

4.3.4. Lithium Phosphate (LiP)

To assess the PXRD results with regard to LiP, the pattern, 00-015-0760, was applied. This compound could not be identified with sufficient confidence. With the EPMA, a phase was analyzed that contained only P and small amounts of Al and Si (Appendix A, Table A3). The P value matches very closely to that of Li_3PO_4. The grains of this phase are hypidiomorphic, and they have irregular cracks and other damages (Figure 4).

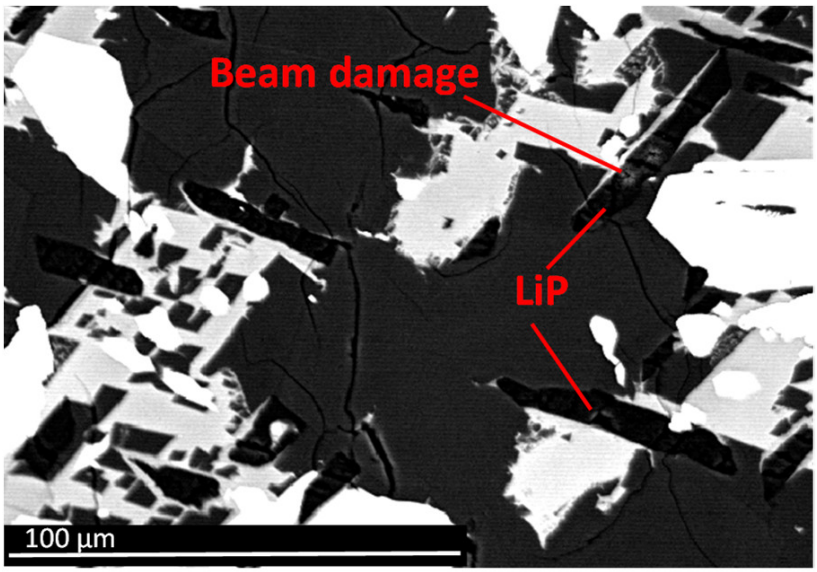

Figure 4. BSE(Z) micrograph of a section containing very dark and irregularly shaped LiP, with cracks and beam damage in ASSB-7.

4.3.5. Eucryptite-Like Alumosilicate (Ec (EcP)) and Li Silicates

To evaluate the PXRD results with respect to Ec (EcP), the pdf-2 pattern, 01-075-2330, was used (Figure 5). This compound could be verified in ASSB-1 and ASSB-10. ASSB-1 contains distinctively more Ec than ASSB-10. In ASSB-7, there is only a slightly elevated background, which possibly indicates a small amount of Ec (<<2 wt.%). The elevated background is quite broad (0.43 °2θ or 0.05 Å), which is eventually due to the solid-solution-like variation in the lattice constants.

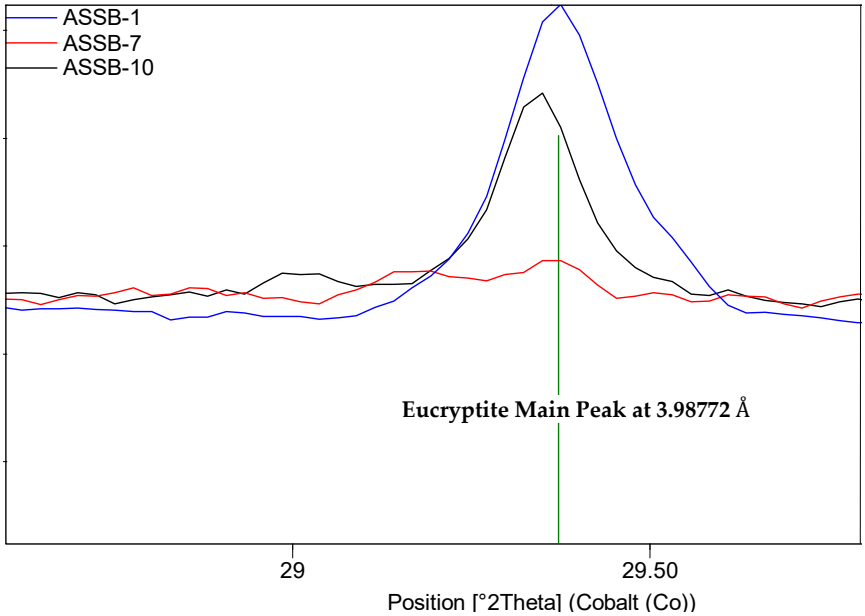

Figure 5. Section of PXRD measurements, with the main peak of Ec.

The EPMA reveals that the Li aluminosilicate can incorporate P (Appendix A, Table A4). The calculations lead to two variations: nearly pure $LiAlSiO_4$ in ASSB-1 and ASSB-10, and an Al-depleted variant with excess Li with the general formula, $Li_{1+x}Al_{1-4/3y}Si_{1-1/4x+y-z-}P_{4/5z}O_4$, with P, in ASSB-7. Because of the similar mean atomic numbers, the Li aluminosilicate is difficult to distinguish from the LiAl in the BSE(Z).

The grains seem to be more hypidiomorphic and massive and without skeleton growth. In ASSB-1 and ASSB-7, the grains of Ec are difficult to find, are very small, and are distributed in the matrix. Only in ASSB-10 can larger grains be found (Figure 6). In ASSB-10, another Li aluminosilicate (with the formula: $Li_2Al_2SiO_6$) was found with single-point analysis (Table A5). In ASSB-1 and -7, a virtual Li silicate, such as Li_2SiO_3, Li_4SiO_4, or $Li_2Si_2O_5$, could be calculated to balance the remaining Li and Si of the bulk chemical composition. These compounds could not be verified via PRDA or EPMA.

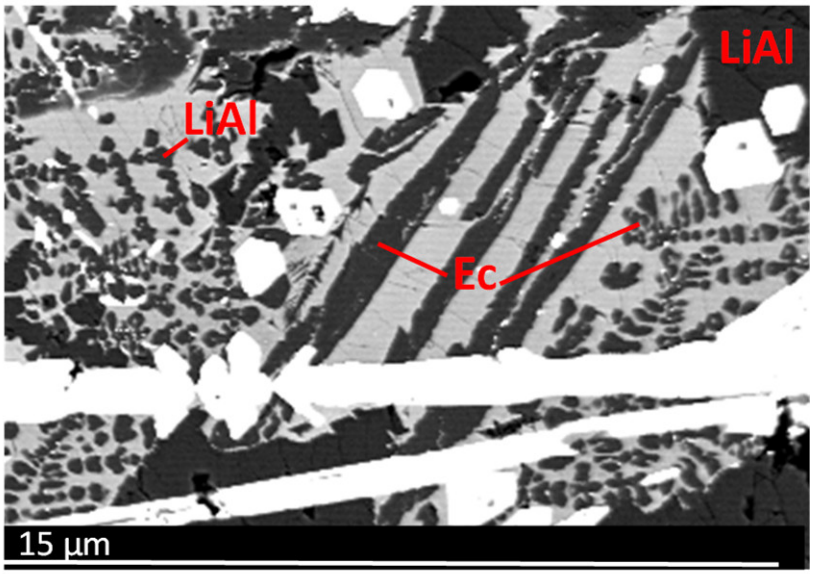

Figure 6. BSE(Z) micrograph of a section containing lath-shaped xenomorphic grains of Ec in ASSB-10.

4.3.6. Perovskite Solid Solution (Pv)

The evaluation of the PXRD results with respect to Pv was carried out with the pdf-2 patterns of $La_{0.66}TiO_{2.993}$ (00-026-0827), $CaTiO_3$ (01-075-2100), and, for comparison, $La_2Zr_2O_7$ (01-071-2363). In this case, the situation is more complex because the Pv peaks are between $CaTiO_3$ and $La_{0.66}TiO_{2.993}$ (Figure 7, blue line). Additionally, the main peak is theoretically overlapped by a peak of the PyC solid solution. By comparing the Py and PyC main peak regions, it can be seen that no signal in the pyrochlore (i.e., PyC) region is detectable in ASSB-1. Additionally, no pyrochlore-like compound was found in ASSB-1 with the EPMA. In ASSB-7 and -10, on the other hand, no signal was detectable in the range of $La_{0.66}TiO_{2.993}$. From this, it can be deduced that ASSB-7 and -10 do not contain any Pv, which is further supported by the fact that both samples do not contain Ti, and, with the EPMA, no perovskite-like compound was found. Conversely, this means that the peak at 2.693 Å in the diffractogram of ASSB-1 does not stem from the PyC solid solution, but most probably from the Pv solid solution. Interestingly, the split peaks within the region between $CaTiO_3$ and $La_{0.66}TiO_{2.993}$ indicate two generations of perovskite, one more La-dominated, and another more Ti-dominated. The EPMA results show a solid solution of XYO_3, with the calculated general formula, $Ca_{1-w}La_{2/3w}Ti_{1-(x+y+z)}Al_{4/3x}Zr_yTa_{4/5z}O_3$ (Appendix A, Table A6). The habitus of this perovskitic oxide is hypidiomorphic to xenomorphic, and it forms not only single large crystals, but also small grains within the matrix.

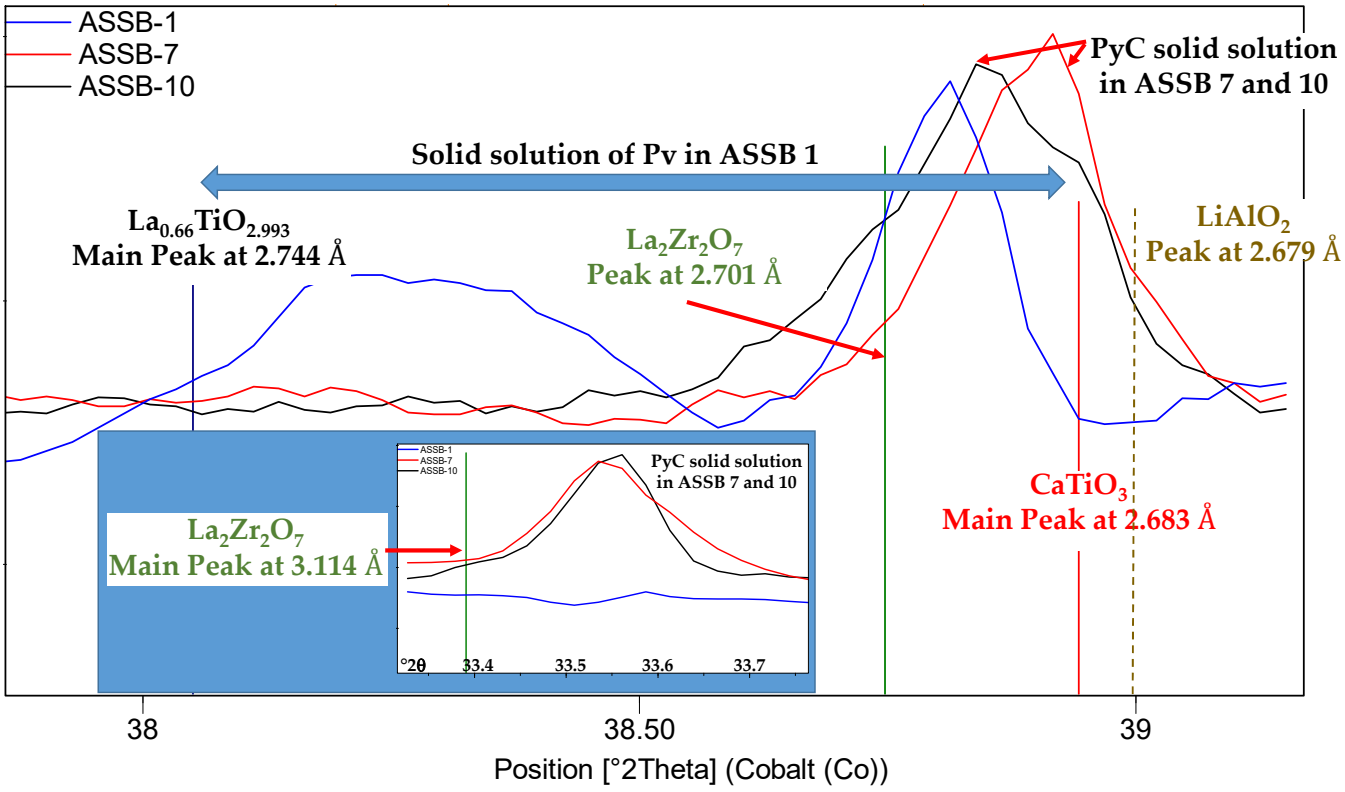

Figure 7. Section of PXRD measurements with the main peaks of $La_{0.66}TiO_{2.993}$, $La_2Zr_2O_7$, $CaTiO_3$, and LiAl (from left to right).

4.3.7. Zirconate Solid Solution (ZrC)

The Zr-rich oxides are difficult to evaluate with PXRD because of the low concentrations. To evaluate the occurrence of Zr-rich oxides, the pdf-2 patterns of $CaZrO_3$ (01-075-0358) and ZrO_2 (01-080-0966) were selected (Figure 8). Unfortunately, in the angular region of the Zr-oxides there are line overlays with the La-silicates (OxS and BpHS).

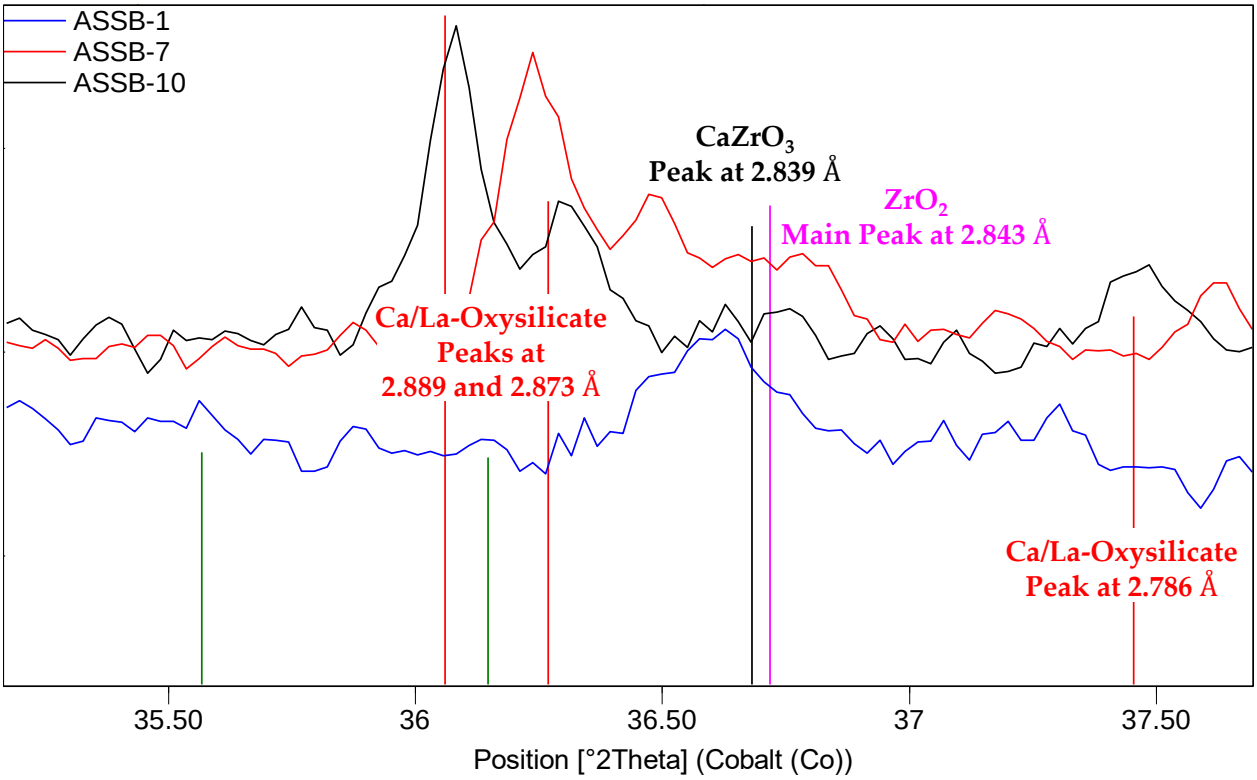

Figure 8. Section of PXRD measurements with the main peaks of Ca/La oxysilicate, britholite, $CaZrO_3$, and ZrO_2 (from left to right).

There is an indication of Zr-rich oxides in ASSB-1, and maybe in ASSB-7, whilst in ASSB-10, this region is very close to the background count rate. The EPMA results reveal a solid solution that is best calculated on a XY_4O_9 (Ca-zirconate) basis, with the general formula being: $Ca_{1-w}La_{2/3w}Zr_{4-(x+y+z)}Al_{4/3x}Ti_yTa_{4/5z}O_9$ (Appendix A Table A7). Titanium is only present in ASSB-1. In ASSB-1, this compound has a hypidiomorphic habitus and a small grain size (5–10 µm). In ASSB-7, the appearance of this phase is very different. In this case, the zirconate, or Zr oxide, always forms cross-formed lamellae in the center of a pyrochlore grain (Figure 9).

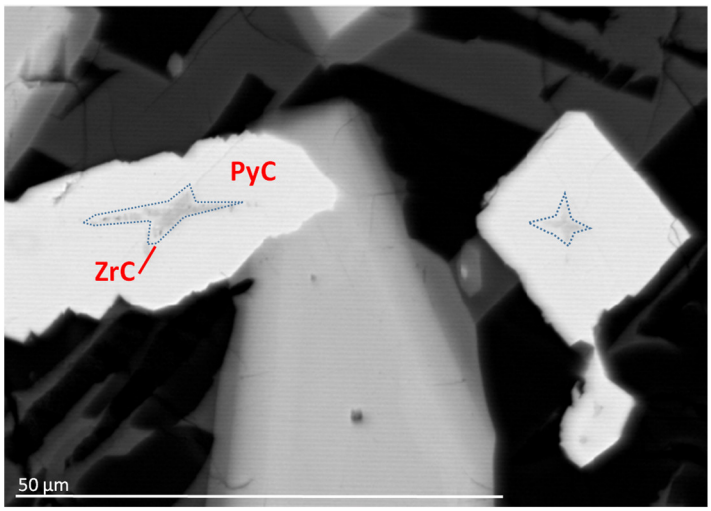

Figure 9. BSE(Z) micrograph of pyrochlore grains in ASSB-7 with zirconate lamellae in the center.

4.3.8. Pyrochlore Solid Solution (PyC)

To evaluate the PXRD results with respect to the PyC, the pdf-2 pattern of $La_2Zr_2O_7$ (01-071-2363) was used. Because of the line overlaps with the Pv, the result is already presented in Figure 7. The Ti-bearing sample, ASSB-1, does not contain this phase. The distinct deviation of the measured lattice spacing from the (222)-plane of the $La_2Zr_2O_7$ pattern of 0.015 Å of both ASSB-7 and ASSB-10 is remarkable. This indicates a pyrochlore-like solid solution instead of pure $La_2Zr_2O_7$, with comparable compositions in ASSB-7 and ASSB-10. The EPMA results confirm this observation of a pyrochlore-like solid solution, with similar chemistries in ASSB-7 and ASSB-10, and with the general formula being: $La_{2-x}Ca_{3/2x-y}Zr_{2+2/4y-z}Ta_{4/5z}O_7$ (Appendix A Table A8). The habitus of this phase is idiomorphic to hypidiomorphic. In ASSB-7, the center nearly always contains a cross-formed lamella of zirconate, which is missing in ASSB-10. The shape of the idiomorphic crystals is very similar to that of the spinel grains, but it is slightly distorted, which indicates the defect fluorite structure reported in [53].

4.3.9. Oxysilicate and Britholite-Like Phosphosilicate (OxS and BphS)

OxS and BphS are not easily resolved in the PXRD pattern. To assess the occurrence of these phases, the pdf-2 patterns of the structurally very similar compounds, calcium lanthanum oxide silicate (01-071-1368) and britholite-(La) (01-076-0339), both of which are hexagonal, were used (Figure 8). Due to line overlaps with OxS and BphS, the PXRD is already presented in Figure 8 of chapter 4.3.7. Monoclinic La_2SiO_5 (00-040-0234) could not be assigned, doubtless because of the PXRD measurements. Because of the potential line overlays with the Zr oxides, the lines of ZrO_2 and $CaZrO_3$ are also shown (Figure 8).

Interestingly, this type of britholite-like silicate occurs both in ASSB-7 (with P) and ASSB-10 (without P), and it is therefore independent of the presence of P. Despite the distinctively lower concentrations of Zr, La, and Ta, the absence of these phases in the P- and Ti-containing ASSB-1 indicates that the reason for this absence may be the formation of perovskite in the presence of Ti, and the subsequent depletion of La during the solidification process.

By looking into the main PXRD peaks of the OxS and BphS, the presence of BphS cannot be clearly verified. The three peaks at 2.89, 2.87, and 2.79 in ASSB-10, which are clearly assignable to OxS, are shifted by 0.15 °2θ or 0.012 Å towards smaller lattice distances in the P-containing ASSB-7. This is an indication of the slightly changed chemical composition, which may be caused by the presence of P in ASSB-7. Thus, to synchronize the chemical composition of the point analysis with the stoichiometry, the formula of the best-fitting pattern ($CaLa_4(SiO_4)_3O$) could be used. However, the EPMA chemical data reveals that, in ASSB-10 and ASSB-7, there occurs a La-rich siliceous compound that can be derived from La_2SiO_5 with the exchange of La→Ca (in ASSB-10), or the exchange of La→Ca and Si→P (in ASSB-7), and the general formulas: $La_{2-(x+y)}Ca_{3/2x}Si_{1+3/4y}O_5$ and $La_{2-x}Ca_{3/2x-z}Si_{1-y+1/2z}P_{4/5y}O_5$ (Appendix A, Table A9). The calculation of the general formula implies that the substitution/charge balance mechanism is not simply Ca^{2+}→La^{3+}/P^{5+}→Si^{4+} (ASSB-7) or $2La^{3+}$→$3Ca^{2+}$ (ASSB-10), as this leads to a distinct chemical imbalance that synchronizes the stoichiometry with the chemical result.

The grains/crystals of the pseudohexagonal-looking OxS in ASSB-7 and ASSB-10 are prismatic structures with massive-looking crystals, without segregation lamellae or accretion streaks. The crystals of the P-free OxS in ASSB-10 seem to be more elongated and lath-shaped (Figure 10). Interestingly the grain/crystals of OxS in ASSB-7 are always surrounded by BphS. The habitus of OxS is mostly idiomorphic, which indicates crystallization in an early step of the solidification.

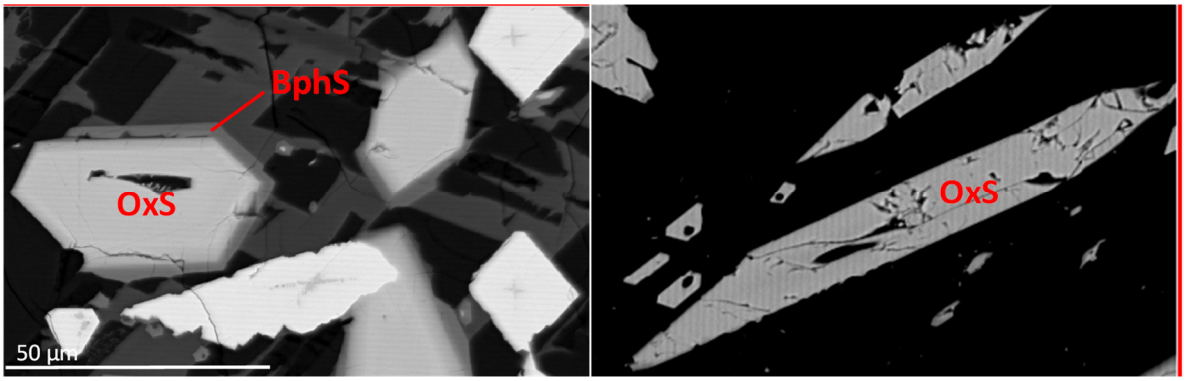

Figure 10. BSE(Z) micrograph of OxS/BphS grains in ASSB-7 (**left**), and OxS grains in ASSB-10 (**right**).

An element distribution profile shows a sharp but still continuous transition between BpHS and OxS, indicating a (limited) solid solution (Figure 11).

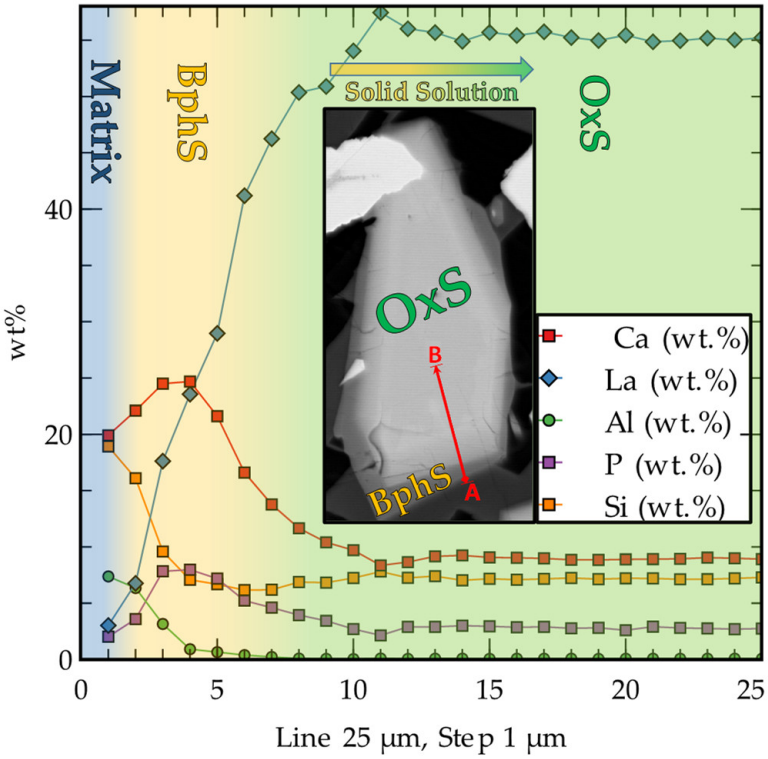

Figure 11. Element distribution profile of a phosphosilicate grain in ASSB-7. Explanations are in the text.

The sample, ASSB-7, additionally contains La- and Ca-rich phosphosilicate (here, BphS), with Ca: La~1: 1 and Si: P~1: 1, in terms of the wt.%, with a general formula of $Ca_{5-v}La_{2/3v}P_{3-(w+x+y+z)}Al_{5/3w}Si_{5/4x}Zr_{5/4y}Ta_zO_{11}$, which can be derived from apatite ($Ca_5(PO_4)_3$(F, OH, Cl)) (Appendix A, Table A10). This phase encloses the grains of the La-rich OxS, but they can also occur as single grains. These grains look more hexagonal than those of the OxS in ASSB-7.

4.3.10. Matrix (Mx1)

Because of the fact that the matrix consists of amorphous, quasiamorphous, or cryptocrystalline constituents, the PXRD does not provide evaluable signals. The EPMA chemical data reveal that the matrix can be highly variable and that it contains all the elements

involved (Appendix A, Table A11). In all the samples, the matrix makes up about a 19–27 wt.%.

The balanced Li concentration increases from ASSB-1 and ASSB-7 to ASSB-10. Aluminum, an important factor for the enrichment of Li (Sp, LiAl, Ec/EcP) has the lowest bulk concentration in ASSB-7, whereas the aluminum contents of the other two samples are comparable. Additionally, the matrix in ASSB-1 has by far the lowest aluminum content. As a result, the total content of the of Li-, Al-, (and Si)-containing phases in ASSB-1 is the highest (about 51 wt.% vs ~40 wt.% in ASSB-7, and ~45 wt.% in ASSB-10).

The average Zr content in the matrix measurements is comparable in ASSB-7 and -10 (~2.9 wt.%), whereas, in ASSB-1, there is no Zr remaining. Therefore, according to the calculation, this element is completely bound in perovskite and zirconate in the slag containing Ti. This may also be because this sample contains very little Zr (0.9 wt.% vs. 4.6 and 4.2 wt.% in ASSB-7 and ASSB-10, respectively).

The average La content in the matrix measurements is the lowest in ASSB-7. Therefore, La seems to be effectively scavenged by the PyC and the La phosphosilicates. In the P-free ASSB-10, the proportion of La transferred into the matrix is higher, which indicates that, without P, the scavenging of La via silicates is less efficient. This is also indicated by the higher amount of calculated siliceous La compounds in ASSB-7 (~17 wt.% vs ~9 wt.% in ASSB-10).

In ASSB-1, the tantalum behaves similarly to zirconium, and it is almost completely scavenged by perovskite and zirconate. Here, too, the low content of the element in ASSB-1 should be noted. In the other two samples, about 1 wt.% of Ta is transferred into the matrix.

Additionally, the matrix in ASSB-1 is particularly noticeable because of the high phosphorus concentration (16.2 wt.%). Therefore, in this case, it can be assumed that the phosphorus has quantitatively accumulated in the matrix. Here, too, the high P/El ratio, i.e., the low contents of Zr, La, and Ta relative to the other samples, may play a role. In ASSB-7, with the same phosphorus content, on the other hand, there is comparatively little phosphorus in the matrix (2.6 wt.%). ASSB-10 contains no P.

4.4. Distributions of Li, Ti, Zr, La, and Ta

In this section, the distribution of the elements among the compounds is presented and is broken down by the individual SyS of ASSB-1, ASSB-7, and ASSB-10.

To calculate the phase composition and to assess the distribution of the interesting elements to these phases, a semiquantitative approximation was calculated by using the average chemical composition of the compounds that were analyzed with the EPMA. An index element was selected for the calculation of the individual quantitative phase fractions (e.g., Ti for Pv: Pv(Ti)). Then, a suitable sequence was selected for the calculation of the phase fractions. This order for the phases and the index elements in ASSB-1, for example, was: Pv(Ti)—ZrC(Zr) Sp(Al); LiAl(Al)—Ec(Al)—Mx(P); and Li silicate(Li).

For more complex relationships, such as the calculations of Sp, LiAl, and Ec using only one element (Al, in this case), a goal seek/solver that is similar to as it is built in Excel® as the "Goal Seek" or "Solver" [80] is used. The constraint for the target value search was chosen to be the optimization of the total sum of the phase composition ("Tot." as wt%) in combination with the optimization of the balance of the calculated element concentrations. In the case of ASSB-10 (Abb 12), the result was: Tot.: 99.6 wt.%, and 100% recoveries for Li, Ti, Zr, and Ta, as well as a 99.96% recovery for La. For the calculation of the Li-bearing phases, the ratio of the compounds estimated with PXRD was used as the starting value. Because the Li estimate for the matrix was calculated as a balance (see Section 3.2.3), the potential Li concentration in the matrix contains a larger uncertainty factor, which may be responsible for the poorer balanceability of the Li (Figure 12).

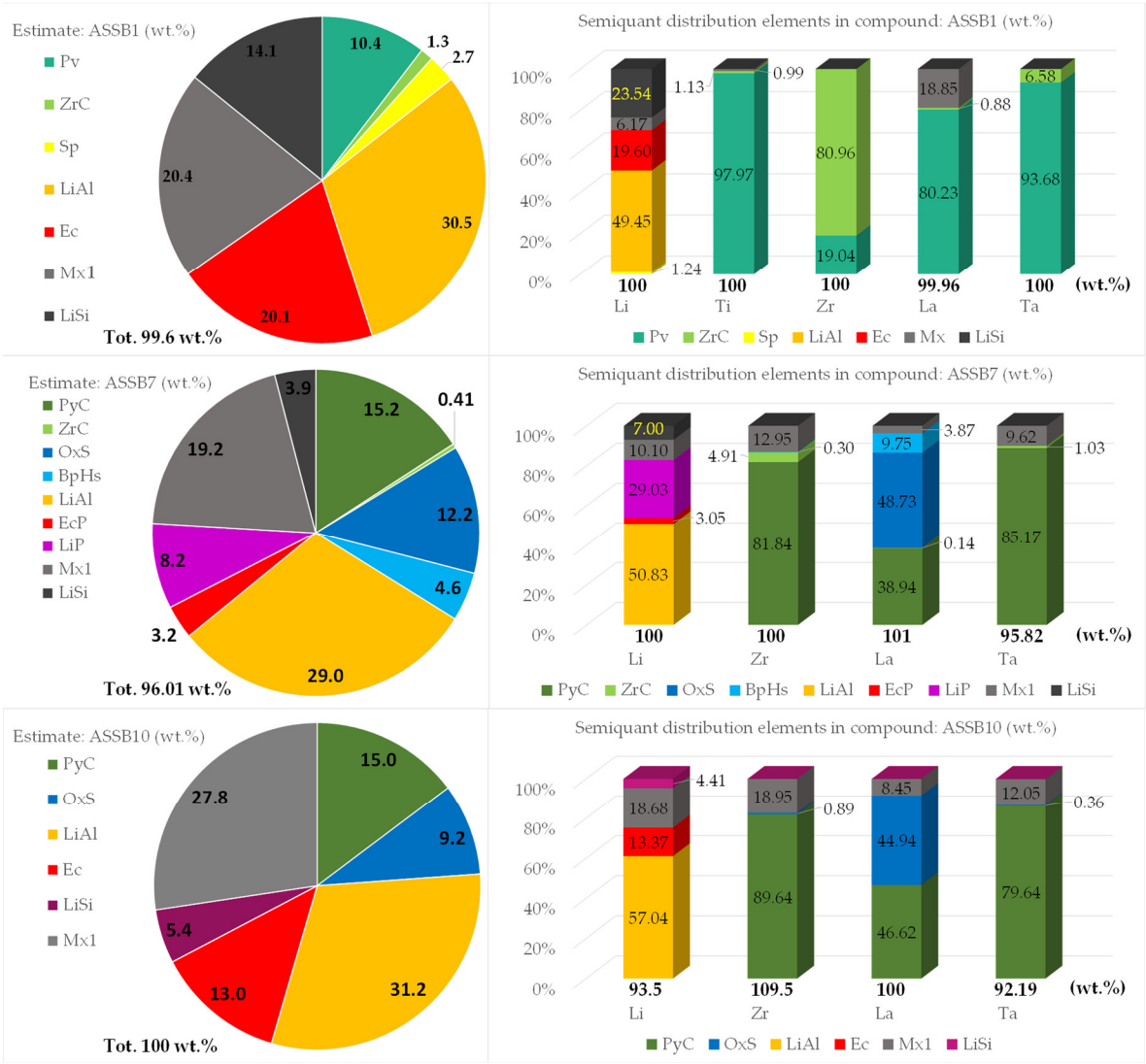

Figure 12. Phase compositions and distributions of elements among the main phases of the samples, ASSB-1, ASSB-7, and ASSB-10. The LiSi (dark grey) in ASSB-1 and ASSB-7 are virtual compounds ($Li_2Si_2O_5$) that belong more to the matrix. The LiSi (violet, ($Li_2Al_2SiO_6$)) in ASSB-10 is derived from real measurements.

In the presence of Ti (ASSB-1), perovskite incorporates titanium nearly completely, and the elements: Zr to about 19%; La to about 80%; and Ta to about 94%. Zirconate incorporates about 80% Zr, approx. 1% La, and approx. 7% Ta. The Ti incorporated in zirconate plays no significant role because of the small content of this phase (1.3 wt.% zirconate in ASSB-1). The matrix incorporates a substantial amount of La (~19%).

Lithium behaves distinctly differently. Most of this element is located in LiAl (~49% Li) and Ec (19. % Li). A smaller amount can be found in the matrix (~6% Li) and Sp (~1% Li). Unfortunately, only ~77% of the bulk Li (5.6 wt.% in ASSB-1) could be directly calculated. Together with the fact that, after the calculation, the Si could also not be allocated to 100%, this is an indication that the sample could contain a Li-silicate compound, such as Li_2SiO_3, Li_4SiO_4, or $Li_2Si_2O_5$. In this case, the calculation of the additional virtual $Li_2Si_2O_5$ (~24% Li) gives the best overall phase balance (99.6 wt.% phases). Nevertheless, neither the PXRD nor the EPMA results give a clear indication of such a compound. Phosphorus, which is also present in the sample, accumulates in the matrix, together with Ca.

If the material does contain P but no Ti (ASSB-7), most of the Zr (~82%) and Ta (85%) are incorporated into the PyC. Additionally, this compound contains about 39% of the La.

Most of the La is distributed over the (phospho-)silicates, OxS (~49%) and BphS (~10%). The matrix contains about 4% of La.

Lithium, again, forms different compounds. In ASSB-7, ~51% of the Li is accumulated in LiAl, ~3% in EcP, and ~29% in LiP. The matrix contains about 10% of the bulk Li. In this sample, ~94% of the bulk Li (5.1 wt.%) could be calculated. As in ASSB-1, a small quantity of Li and Si could not be allocated to the described phases. In this case, the calculation of the additional virtual $Li_2Si_2O_5$ (~7%Li) gives the best overall phase balance (100 wt.% phases). Moreover, in this sample, neither the PXRD nor the EPMA results provide a clear indication of such a compound.

If the sample contains neither P nor Ti (ASSB-10), such as in the P-containing ASSB-7, then most of the Zr and Ta is concentrated in the PyC (90 or 80%, respectively). Here, about 45% of the La is incorporated in this phase. The silicate phase (here, only OxS) contains about 45% of the bulk La. The rest of the La is located in the matrix (~9%).

Moreover, in this sample, lithium forms its own compounds. Here, 57% of the bulk Li is concentrated in LiAl, and ~13% in Ec. In this sample, a small amount of a different Li aluminosilicate ($Li_2Al_2SiO_6$) was found, which was accumulating about 4.4% of the bulk Li. The rest of the Li is accumulated in the matrix (~19%). In this sample, ~94% of the bulk Li (5.1 wt.%) could be calculated. In this case, there is no further indication of a missing Li compound. For unknown reasons (with regard to the measurements), the balancing of the elements in this sample–especially for Zr—shows a larger deviation.

Since the phase composition of the matrix is not known, it is possible that some parts of the compounds are cryptocrystalline, and that they therefore cannot be calculated as a proportion of these compounds.

5. Discussion

The phase formation and the incorporation of the elements into these phases provide important information on the behavior of slag systems upon the addition of additives. In this case, the reaction of the important commodity elements, Li, Zr, La, and Ta, in a synthetic slag-like Al/Si/Ca environment, with the addition of additives such as Ti and P, was investigated. All these elements potentially occur in the slags from battery recycling.

A first important observation is that, on the basis of the calculations (because Li is not measurable), Li forms its own compounds only with Al, Si, and P. Although Li-containing compounds, such as LLZ or LATP, can be synthesized, there is no evidence that Li behaves equally in the SyS. With respect to the Li in all the samples, the LiAl based on the general formula, XYO_2 (X: Li; Y: Al(Si)), is predominant. As was observed earlier by Schirmer et al. [24], this compound always contains silicon. This confirms that a limited solid solution exists with the substitution of $1Li^+ + 1Al^{3+} \leftrightarrow 1Si^{4+}$. Looking onto the average values for the Si in the LiAl in all three samples (total n = 66), the maximum solubility of Si is about 10 wt.%.

Li alumosilicates (Ec, EcP), which were based on the general formula, $XYZO_4$ (X: Li; Y: Al; Z: Si(P)), occur in all the samples, but in presence of P without the addition of Ti, they can be strongly suppressed and contain P. The results show that P can be incorporated into the $LiAlSiO_4$ lattice. If P is substituting Si, and the charge balance is realized with Al, the Al concentration should be higher than in normal eucryptite. This is not the case in ASSB-7, but the calculated lithium content is higher than in pure eucryptite, and it is coupled with a lower aluminum content. With the assumption that not all of the Li positions in normal eucryptite are occupied, a charge balance that is based on excess Li is plausible.

In ASSB-7, Li seems to have a distinct affinity to P, and it forms LiP on the basis of the general formula, X_3YO_4 (X: Li; Y: P(Si). This situation may have something to do with the distinctively lower amount of bulk Si and Al in ASSB-7 (8.9 and 11.9 wt.%, respectively) and the early crystallization of the OxS and BphS that scavenge the Si from the melt in an early stage. These two factors, together with the scavenging of Al and Si through LiAl, could lead to a lack of Si and Al in the melt. Although P is also incorporated into the BphS, this element appears to have accumulated in the residual melt. Therefore, a Li-rich P-dominated

residual melt may have formed, which leads to the crystallization of the LiP. The fact that parts of the Si, Al, and Li, and all of the Ca are remaining at the end of the calculation (i.e., in the matrix) is an indication that this P-rich melt has separated from the remaining liquid phase, and that it may be leaving a second Li-rich siliceous eutectic melt at the very end of the solidification. If this were true, the solubilities of Si, and especially of Al and Ca, would have to be very low in this melt. It should be noted, however, that these calculations could only serve as an estimation. If the incorporation of lithium into aluminate or eucryptite is desired, the presence of P is counterproductive to the processing of this element. Therefore, it is possible that the simultaneous removal/processing of La, where the P increases the efficiency, and Li, where the P leads to undesirable phase formations, would be difficult.

The behavior of the elements, Zr, La, and Ta (besides the bulk concentrations), strongly depends on the formation of perovskite. Perovskite, with the basic formula, XYO_3 (X: Ca, La; Y: Ti, Zr, Ta), forms only in the presence of Ti, which almost quantitatively removes the Ti from the melt. In the sample, ASSB-1, except for the matrix, La and Ta are predominantly enriched in the Pv compound. The PyC was not detectable, probably because the La accumulated mainly in the Pv. In this sample, the Zr is mainly scavenged by ZrC, most probably through the suppression of the PyC because of the scavenging of La via the Pv. This is interesting because, compared with the Pv, the PyC is the phase with the higher melting point (~2300 °C vs 1964 and 1970 °C). If the low content of Zr in ASSB-1 is not responsible for the absence of the PyC, this could mean that an affinity of Ti, La, and Ca already exists in the melt, before the solidification of the slag, and that, thus, the formation of the higher melting compound is suppressed.

If Ti is missing, Zr and Ta, together with about 40 wt.% of the La, are enriched in the PyC, with the general formula: $X_2Y_2O_7$ (X: Ca, La; Y: Zr, Ta). This, of course, depends on the ratio of the three elements in ASSB-7 and ASSB-10. Because, in ASSB-7, a minor part of Zr is forming zirconate in this sample, the maximum amount of La available to remove the total amount of Zr (4.6 wt.%) via the PyC has been exceeded, possibly through a lanthanum-consuming competitive reaction. From the BSE(Z) micrographs (Figure 2, Figure 8, and Figure 10), it is clear that the La (phospho)silicates are early crystallizates, and that they therefore compete with the PyC for the incorporation of compatible elements during solidification.

When looking at the BSE micrographs of the PyC in the sample, ASSB-7, the impression arises that, at the beginning of the crystallization, the excess Zr is incorporated into the structure (Figure 8). After cooling down, the PyC is breaking apart, and, therefore, in the center of each crystal that was formed at an early stage of the solidification with the excess Zr, a cross-shaped segregation lamella of zirconate is formed. Fabrichnaya et al. [51] give a limited solid solution for the PyC, at least in the binary system, La_2O_3—ZrO_2, which is not stable at room temperature. To what extent calcium may play a role is not known.

Obviously, this is not the case in ASSB-10, because no zirconate segregation lamellae were found in the center of the PyC crystals. Together with the observation that relatively more La silicates (OxS and BphS) are calculated in ASSB-7, this allows one to conclude that the scavenging of La through these phases starts at an earlier stage in ASSB-7 than in ASSB-10. Thus, the ratio of La to Zr in ASSB-10 at this solidification stage was more favorable for the formation of pyrochlore. Furthermore, this could mean that phosphorus-containing La silicates (esp. OxS) crystallize earlier upon cooling, which indicates a higher melting point.

As was mentioned above, in the absence of Ti, La also forms silicates, in addition to an oxidic compound. If P is also not present, OxS, with the general formula, X_2YO_5 (X: Ca, La; Y: Si), is formed (ASSB-10). In this sample, OxS is scavenging about 45 wt.% of La from the melt. Since this compound contains about half of the lanthanum, it is considered an important competitive reaction for the formation of the PyC.

In the presence of P (sample ASSB-7), the situation is more complex because of the formation of two different types of La silicates, both of which contain phosphorus. These two compounds show all the signs of a more or less completely solid solution. While pure La_2SiO_5 is generally referred to as “monoclinic” in the literature, all britholitic compounds

(with or without P) are referred to as "hexagonal". This would make a phase mixture of this type seem unlikely. The BSE micrographs in ASSB-7 reveal that the combined OxS/BphS crystals have a distorted hexagonal shape. Part of this distortion is probably due to the cutting angle of the grains. Besides this fact, it would be possible to assume that there is only a small difference between the hexagonal lattice (BphS) and a (potential) pseudohexagonal monoclinic lattice (OxS with P) enabling a (limited) solid solution. As there is no fundamental difference in the bulk La concentrations in ASSB-7 and -10 (13.9 vs 12.3, respectively), the OxS/BphS appears to be more efficient than the P-free OxS, accumulating nearly 60 (OxS + BphS, ASSB-7), instead of 45, wt.% (only OxS, ASSB-10). If Ti and Zr (and Ta) are missing, it is most probable that La will be exclusively scavenged by OxS and—if P is present—by OxS and BphS.

The matrix is a massive, but extremely fine-grained, cryptocrystalline/pseudoamorphous-to-amorphous mixture that, in principle, can contain all the compounds that are determined as large grains or crystals, as well as amorphous compounds, such as glass. The chemistry can be more variable, it represents all the elements, and it does not follow any stoichiometric constraints, and so it is difficult/impossible to calculate a consistent formula. The measurement total is often quite low, which is most probably due to the microporosity of the fine-grained mixture and the possible lithium concentration, which, in this case, was to be calculated as a balance, and it therefore contains a higher uncertainty factor. Additionally, a large number of measurements had to be omitted because of very poor totals. Therefore, this component complicates the calculations, and it represents an uncertainty factor.

The matrix accounts for about 19 to 27 wt.%, with the highest content in ASSB-10, and comparable contents in ASSB-1 and ASSB-7. Despite the overall significantly smaller grain sizes, the calculated percentage of the matrix in ASSB-1 is comparably low. The remaining element concentrations in the matrix can be a measure of the efficiency, with the elements being incorporated into the mineral compounds, with processable grain sizes. This depends on the total concentration of the element, the concentration of the other elements that are present in the compound, and the efficiency of the incorporation of the element into the compound. A very clear example is the situation in ASSB-1. Because of the presence of Ti, a perovskitic oxide was forming. This oxide is extremely efficient at removing Ti from the solidifying melt. The residual concentration in the matrix is about zero. Almost as efficient is the scavenging of Ta, which, additionally, is also because of the comparably low concentrations. Zirconium, on the other hand, is very efficiently incorporated into zirconate. The incorporation of La into Pv or ZrC is less efficient, and it leaves about 19 wt.% of this element in the matrix. In this case, about 100 wt.% of the Ti, Zr, and Ta can be transferred to the mineral/crystalline phases, whereas 19 wt.% of the La will be lost because of its location in the very fine-grained matrix.

If Ti is missing, the presence of P can help to increase the incorporation of La into the processable mineral compounds/crystals via the formation of phosphosilicates besides the PyC, although the effect of P is by far not as pronounced as is documented in [18]. In the presence of Zr, the PyC is an appropriate scavenger, especially for Ta (besides Zr), although it may be less efficient than perovskite. ZrC seems to form when the incorporation capacity of the other phases, such as the PyC, for this element is exceeded. This may depend on the maximum concentration of the element in the phase, and on the maximum phase concentration in the material.

Since the phase composition of the matrix is not known, it is of course possible that part of the zirconate is cryptocrystalline, and that therefore it cannot be calculated as a proportion of the ZrC.

To clarify this, the solidification of the two samples with comparable Zr and Ta concentrations, and with or without Ti, should be investigated.

The overall morphology of the slag samples gives an indication of the order in which the compounds crystallized upon cooling. The early crystallizates show a mostly idiomorphic habitus, co-crystallizing/competing phases, and a hypidiomorphic-to-xenomorphic habitus, and the residual crystallizates show a xenomorphic habitus that is combined with

small grain sizes. Furthermore, the dendritic or skeletal appearance may indicate very rapid growth that is due to the undercooling/oversaturation or segregation of the melts. If large crystals form from a few nuclei at an early stage of the solidification, this could be (thermodynamically) advantageous for the further growth of crystal blocks or structures onto the comparably large surfaces of these large crystals.

In the case of ASSB-1, the idiomorphic Sp crystals are immediately recognizable as early crystallizates. The Pv forms larger grains with rudimentary hypidiomorphic structures. Because of the size of the grains, it can be assumed that this compound is also crystallized relatively early, with a comparatively low nucleation rate. The skeletal LiAl grains with a partially hypidiomorphic habitus indicate the distinct undercooling of the melt during crystallization. These structures were probably formed at lower temperatures in the melt. The finely structured matrix then represents the eutectic residual crystallization. In this sample, the cooling curve resulted in a suboptimal morphology, with few usable large crystals.

Typical of ASSB-7 are the idiomorphic and isometric PyC crystals, and the more or less isometric pseudohexagonal-monoclinic La phosphosilicate crystals (OxS/BphS), which indicates that these phases are early crystallizates that will eventually compete with each other. In this sample, the LiAl crystals are also hypidiomorphic, with a relatively small amount of dendritic or skeletal structures. Between the LiAl crystals are gusset fillings with LiP, which indicates that this compound formed from a residual eutectic melt. Because of the high purity of the component with the main element (P), and only small amounts of Si and Al, it is even conceivable that this is the residue of a phosphate-rich second melt. In ASSB-7, fewer small dendritic or skeletal structures have formed. This is more advantageous for processing. Unfortunately, a large amount of Li could be lost through the formation of Li_3PO_4.

Typical of ASSB-10 are the elongated lath-like monoclinic-looking OxS crystals, some of which are cut transversely, thereby forming isometric-looking cross sections. The shapes of the phosphor-free OxS crystals/grains seem to be more elongated than the those of the OxS/BphS crystals/grains in ASSB-7. This would complicate the liberation for further processing via flotation. In contrast to ASSB-7, the PyC crystals form skeletal structures, which indicate rapid growth. This indicates that the solidification in this sample was different (e.g., compared with ASSB-7), and that the temperature range of the PyC crystallization was traversed very quickly. Since the cooling curve was the same in all the samples, this suggests that the chemism of the melt (such as the presence of P in ASSB-7) has an influence on the crystallization temperature of each phase.

The LiAl crystals in ASSB-10 appear massive, but small skeletal forms also exist, so that two generations of LiAl crystallizations may be present. The small LiAl crystallites could be lost during preparation because of the poor liberability.

Assuming that all the melting experiments were set up in the same way, this would mean that, for the different samples, the start of the crystallization of each compound occurred at different temperatures.

6. Conclusions and Outlooks

In the future, if pyrometallurgical treatment is to be applied to material containing Li, Zr, lanthanides, and Ta, the engineered artificial mineral (EnAM) approach should be considered. This approach deals with the enrichment of the desired elements during the solidification of slags into mineral phases, with the best possible liberability. The first step is to understand the phase reactions by using experiments with synthetic slags. The results can then be used for (nonequilibrium) thermodynamic modeling.

In the presence of Ti, all of the discussed elements are scavenged by mineral compounds that are, in principle, suitable for processing via an EnAM approach. It has to be investigated, in detail, whether there is a cooling curve in which all the phases have advantageous grain sizes and grain shapes.

In the absence of Ti, the addition of P can help to improve the scavenging efficiency for La (and therefore, most probably, also the light REEs, Ce, Pr, and Nd), but at the expense of the processability of Li because of the LiP formation (unless the LiP advances to a potential EnAM).

However, even without the addition of P, similar silicate compounds are formed, albeit with less advantageous grain shapes.

On the other hand, the cubic PyC, or the orthorhombic/tetragonal/cubic Pv, form more isometric crystals, which are certainly easier to liberate through processing.

This would mean that the presence of Ti would be more beneficial than the addition of P. The presence of La (or other light REEs), in turn, would also enhance the recoverability of Zr and Ta via the formation of the PyC, especially in the absence of Ti. To gain more information on the observed reactions, especially with regard to the Pv, ZrC, and PyC interactions, further research is necessary using different synthetic slag mixtures, such as:

(a) Only Ti and La;
(b) Only Ti and Zr/Ta;
(c) Only La and P;
(d) Only La;
(e) Only Li and P.

Additionally, for the standard slag elements, Si, Al and Ca, the application of molecular dynamic modeling could provide results on the preferential precipitation of the Pv over the PyC in the solidification of Ti-bearing slags with La and Zr.

The cooling curves should be assessed as accurately as possible to find the optimal crystallization conditions for the phases/compounds of concern.

Not to be neglected is the investigation of the influence of the element, Mg, since this is automatically introduced in the large-scale process via the impurities of the Ca raw material (e.g., limestone).

It is known that Mg forms spinel, which, as an early crystallizate, competes with the formation of aluminum-rich oxides, such as $LiAlO_2$ or $LiAl_5O_8$. (e.g., [24]).

In order to verify the presence and concentration of the only calculated element, lithium, in the different phases, analytical methods, such as La-ICP-MS or SIMS, should be used, with which Li can be directly determined.

Author Contributions: Conceptualization, T.S.; mineralogical investigation, characterization, interpretation, T.S.; calculations of element distribution and mineral/phase formulas, T.S.; thermochemical modeling, C.S. and B.F.; slag design, subsampling, and preparation, H.Q. and D.G. All authors have read and agreed to the published version of the manuscript.

Funding: This research was funded by the German Federal Ministry of Eductaion and Research in the frame of the "InnoRec" project from the "ProZell" cluster project (project number: 03XP0246A and 03XP0246D).

Acknowledgments: The authors acknowledge the financial support of the German Federal Ministry of Education and the research within the cluster project, "ProZell InnoRec", under the reference numbers: 03XP0246A and 03XP0246D. We thank Petra Sommer, Heike Grosse, and Maike Gamenik from the Institute of Mineral and Waste Processing, Waste Disposal and Geomechanics for their analysis. We additionally acknowledge the support by the Open Access Publishing Fund of the Clausthal University of Technology.

Conflicts of Interest: The authors declare no conflict of interest. The funders had no role in the design of the study; in the collection, analyses, or interpretation of data; in the writing of the manuscript; or in the decision to publish the results.

Appendix A

Table A1. Composition of LiAl (wt.%) based on single-point analysis. Ave.: arithmetic average; Min./Max.: lowest/highest measured values; RD: relative standard deviation (%); N: number of measurements; n.a. not applicable (calculated values), * calculated value.

	ASSB-1				ASSB-7				ASSB-10			
wt.%	**Ave.**	**Min.**	**Max.**	**RD**	**Ave.**	**Min**	**Max**	**RD**	**Ave.**	**Min**	**Max**	**RD**
Al	36.0	34.7	36.9	1.6	35.7	32.8	37.0	2.5	36.8	32.6	38.4	4.0
Si	6.7	5.3	8.1	12.3	6.3	5.1	7.5	9.5	5.7	4.6	9.6	24.4
Li *	9.3	8.9	9.5	n.a.	9.2	8.4	9.5	n.a.	9.5	8.4	9.9	n.a.
N	25				21				20			

Table A2. Composition of Sp (wt.%) based on single-point analysis (only in ASSB-1). Ave.: arithmetic average; Min./Max.: lowest/highest measured values: RD: relative standard deviation (%); * calculated value; N: number of measurements; n.a. not applicable (calculated values).

	ASSB-1			
wt.%	**Ave**	**Min**	**Max**	**RD**
Mg	0.3	0.3	0.4	12.3
Al	49.6	49.0	49.6	0.3
Zn	0.8	0.5	1.1	25.0
Ti	0.3	0.2	0.3	11.3
Li *	2.6	2.5	2.6	n.a.
N	22			

Table A3. Composition of LiP (wt.%) based on single-point analysis (only in ASSB-7). Ave.: arithmetic average; Min./Max.: lowest/highest measured values; RD: relative standard deviation (%); * calculated value; N: number of measurements; n.a. not applicable (calculated values).

	ASSB-7			
wt.%	**Ave**	**Min**	**Max**	**RD**
Al	0.8	0.1	5.2	200.2
P	24.3	21.0	27.9	7.6
Si	1.1	0.6	3.7	74.7
Li *	15.3	14.1	18.8	n.a.
N	15			

Table A4. Composition of Ec (Ec(P)) (wt.%) based on single-point analysis. Ave.: arithmetic average, Min./Max.: lowest/highest measured values; RD: relative standard deviation (%); * calculated value; Li $*_{Ec}$: Ec portion; Li $*_{++}$: Li excess; Li $*_{tot}$: total calculated Li; N: number of measurements; n.a. not applicable (calculated values).

	ASSB-1				ASSB-7				ASSB-10			
wt.%	**Ave**	**Min.**	**Max.**	**RD**	**Ave**	**Min.**	**Max.**	**RD**	**Ave**	**Min.**	**Max.**	**RD**
Al	22.8	20.9	23.6	3.1	18.6	16.1	20.3	5.8	23.5	22.2	24.2	2.2
P	0.2	0.0	0.9	176.1	3.5	2.1	5.1	30.9	0.0	0.0	0.0	n.a.
Si	21.1	20.1	21.8	2.5	19.6	16.7	21.2	6.5	21.0	19.2	22.4	2.9
Li $*_{Ec}$	5.8	5.4	6.1	n.a.	4.8	5.2	4.1	n.a.	6.1	5.7	6.2	n.a.
Li $*_{++}$	Only ASSB-7				2.1	0.4	4.9	n.a.	Only ASSB-7			
Li $*_{tot}$					6.9	5.6	9.0	n.a.				
N	8				17				25			

Table A5. Composition of $Li_2Al_2SiO_6$ (wt.%) based on single-point analysis (only in ASSB-10). Ave.: arithmetic average; Min./Max.: lowest/highest measured values; RD: relative standard deviation (%); * calculated value; N: number of measurements; n.a. not applicable (calculated values).

	ASSB-10			
wt.%	**Ave**	**Min**	**Max**	**RD**
Al	28.1	24.6	31.7	9.1
Si	15.0	13.5	19.2	16.0
Li *	7.2	6.3	8.2	n.a.
N		5		

Table A6. Composition of Pv (wt.%) based on single-point analysis (only in ASSB-1). Ave.: arithmetic average; Min./Max.: lowest/highest measured values; RD: relative standard deviation (%);N: number of measurements.

	ASSB-1			
wt.%	**Ave**	**Min.**	**Max.**	**RD**
Al	1.2	0.6	6.3	86.0
Zr	1.6	0.5	6.0	88.4
Ca	14.7	12.8	16.2	6.6
La	21.0	16.2	24.5	10.4
Ta	3.8	2.7	5.7	20.6
Ti	26.4	20.4	28.5	7.4
N		28		

Table A7. Composition of ZrC (wt.%) based on single-point analysis (only in ASSB-1). Ave.: arithmetic average; Min./Max.: lowest/highest measured values; RD: relative standard deviation (%);N: number of measurements.

	ASSB-1				ASSB-7			
wt.%	**Ave**	**Min.**	**Max.**	**RD**	**Ave**	**Min.**	**Max.**	**RD**
Zr	56.1	0.0	57.5	2.6	55.2	55.1	55.2	n.a.
Ca	7.4	0.1	8.2	6.1	5.7	5.7	5.7	n.a.
La	1.9	0.1	2.0	6.6	4.8	4.6	5.0	n.a.
Ta	2.2	0.0	2.4	5.2	6.7	6.7	6.7	n.a.
Ti	2.5	0.2	2.7	5.2				
N		6				2		

Table A8. Composition of PyC (wt.%) based on single-point analysis. Ave.: arithmetic average; Min./Max.: lowest/highest measured values; RD: relative standard deviation (%);N: number of measurements.

	ASSB-7				ASSB-10			
wt.%	**Ave**	**Min.**	**Max.**	**RD**	**Ave**	**Min.**	**Max.**	**RD**
Zr	24.6	23.2	24.8	1.9	25.2	24.3	26.1	1.3
Ca	3.6	3.4	4.0	4.4	2.8	2.7	3.0	2.5
La	35.7	35.0	36.5	1.6	38.3	36.9	38.8	0.7
Ta	14.7	14.6	15.5	2.8	12.2	11.7	13.4	3.3
N		24				25		

Table A9. Composition of OxS (wt.%) based on single-point analysis. Ave.: arithmetic average; Min./Max.: lowest/highest measured values; RD: relative standard deviation (%);N: number of measurements.

	ASSB-7				ASSB-10			
wt.%	**Ave**	**Min.**	**Max.**	**RD**	**Ave**	**Min.**	**Max.**	**RD**
P	2.9	2.4	3.2	8.7	-	-	-	-
Ca	8.9	8.5	9.3	2.9	5.4	4.9	5.9	5.4
Si	7.3	7.1	7.6	2.2	9.0	7.8	9.3	3.0
La	55.5	54.4	56.8	1.3	59.9	57.4	62.0	1.7
N	17				24			

Table A10. Composition of Bphs (wt.%) based on single-point analysis (only ASSB-7). Ave.: arithmetic average; Min./Max.: lowest/highest measured values; RD: relative standard deviation (%);N: number of measurements.

	ASSB-7			
wt.%	**Ave**	**Min**	**Max**	**RD**
Al	1.2	0.7	1.7	34.9
P	7.9	7.7	8.1	2.1
Zr	0.6	0.3	0.8	46.2
Ca	24.2	22.7	25.2	5.1
Si	7.4	6.7	8.0	8.7
La	24.5	21.2	29.9	18.0
Ta	0.2	0.1	0.3	50.3
N	6			

Table A11. Composition of the matrix (wt.%) based on single-point analysis. Ave.: arithmetic average; Min./Max.: lowest/highest measured values; RD: relative standard deviation (%); * calculated value; N: number of measurements; n.a. not applicable (calculated values).

	ASSB-1				ASSB-7				ASSB-10, Mx1			
wt.%	**Ave**	**Min.**	**Max.**	**RD**	**Ave**	**Min.**	**Max.**	**RD**	**Ave**	**Min.**	**Max.**	**RD**
Al	0.8	0.1	2.3	83.2	6.8	5.2	8.1	9.4	9.5	9.3	12.3	20.7
P	16.2	12.9	17.9	9.4	2.6	2.1	3.3	12	0	0	0	46.7
Zr	0.0	0.0	0.0	0	2.9	2.1	3.7	14	2.9	2.0	3.6	17.5
Ca	31.7	28.6	34.6	6.0	20	19	21	2.4	19.5	16.4	17.8	16.5
Si	3.0	1.2	6.3	52.4	18	17	19	3.1	17.9	17.6	19.4	2.8
La	2.5	1.9	3.5	20.2	2.3	1.5	4.3	28	3.7	3.3	5.3	21.8
Ta	0.1	0	0.2	89.8	1.4	1.1	1.8	14	1.0	0.6	1.1	28.2
Ti	0.1	0.0	0.1	41.9	0	0	0	0	0	0	0	1345
Li *	1.7				2.7		n.a.		3.1			
N	17				29				29			

References

1. Elwert, T.; Goldmann, D.; Schirmer, T.; Strauss, K.W. Phase Composition of High Lithium Slags from the Recycling of Lithium Ion Batteries. *WoM* **2012**, *65*, 163–171.
2. Wittkowski, A.; Schirmer, T.; Qiu, H.; Goldmann, D.; Fittschen, U.E.A. Speciation of Manganese in a Synthetic Recycling Slag Relevant for Lithium Recycling from Lithium-Ion Batteries. *Metals* **2021**, *11*, 188. [CrossRef]
3. Dańczak, A.; Klemettinen, L.; Kurhila, M.; Taskinen, P.; Lindberg, D.; Jokilaakso, A. Behavior of Battery Metals Lithium, Cobalt, Manganese and Lanthanum in Black Copper Smelting. *Batteries* **2020**, *6*, 16. [CrossRef]
4. Fergus, J.W. Ceramic and Polymeric Solid Electrolytes for Lithium-Ion Batteries. *J. Power Sources* **2010**, *195*, 4554–4569. [CrossRef]
5. Janek, J.; Zeier, W.G. A Solid Future for Battery Development. *Nat. Energy* **2016**, *1*, 16141. [CrossRef]
6. Manthiram, A.; Yu, X.; Wang, S. Lithium Battery Chemistries Enabled by Solid-State Electrolytes. *Nat. Rev. Mater.* **2017**, *2*, 16103. [CrossRef]

7. Zheng, F.; Kotobuki, M.; Song, S.; Lai, M.O.; Lu, L. Review on Solid Electrolytes for All-Solid-State Lithium-Ion Batteries. *J. Power Sources* **2018**, *389*, 198–213. [CrossRef]
8. Buschmann, H.; Dölle, J.; Berendts, S.; Kuhn, A.; Bottke, P.; Wilkening, M.; Heitjans, P.; Senyshyn, A.; Ehrenberg, H.; Lotnyk, A.; et al. Structure and Dynamics of the Fast Lithium Ion Conductor "Li7La3Zr2O12". *Phys. Chem. Chem. Phys.* **2011**, *13*, 19378. [CrossRef]
9. Tsai, C.-L.; Ma, Q.; Dellen, C.; Lobe, S.; Vondahlen, F.; Windmüller, A.; Grüner, D.; Zheng, H.; Uhlenbruck, S.; Finsterbusch, M.; et al. A Garnet Structure-Based All-Solid-State Li Battery without Interface Modification: Resolving Incompatibility Issues on Positive Electrodes. *Sustain. Energy Fuels* **2019**, *3*, 280–291. [CrossRef]
10. Kato, T.; Iwasaki, S.; Ishii, Y.; Motoyama, M.; West, W.C.; Yamamoto, Y.; Iriyama, Y. Preparation of Thick-Film Electrode-Solid Electrolyte Composites on Li7La3Zr2O12 and Their Electrochemical Properties. *J. Power Sources* **2016**, *303*, 65–72. [CrossRef]
11. DeWees, R.; Wang, H. Synthesis and Properties of NaSICON-type LATP and LAGP Solid Electrolytes. *ChemSusChem* **2019**, *12*, 3713–3725. [CrossRef]
12. Schwich, L.; Küpers, M.; Finsterbusch, M.; Schreiber, A.; Fattakhova-Rohlfing, D.; Guillon, O.; Friedrich, B. Recycling Strategies for Ceramic All-Solid-State Batteries—Part I: Study on Possible Treatments in Contrast to Li-Ion Battery Recycling. *Metals* **2020**, *10*, 1523. [CrossRef]
13. Qiu, H.; Kersebaum, J.; Wollmann, A.; Feuge, N.; Haas, A.; Goldmann, D.; Wilhelm, R. Improvement of the Froth Flotation of $LiAlO_2$ and Melilite Solid Solution via Pre-Functionalization. *Sci. Rep.* **2021**, *11*, 20443. [CrossRef]
14. Haas, A.; Goldmann, D.; Schirmer, T. Challenges and Research Needs in Flotation of Synthetic Metal Phase. In *Challenges and Research Needs in Flotation of Synthetic Metal Phases*; GDMB Verlag GmbH: Clausthal-Zellerfeld, Germany, 2018; ISBN 978-3-940276-84-1.
15. Bulatovic, S.; Wyslouzil, D.M. Process Development for Treatment of Complex Perovskite, Ilmenite and Rutile Ores. *Miner. Eng.* **1999**, *12*, 1407–1417. [CrossRef]
16. Wang, W.; Zhu, Y.; Zhang, S.; Deng, J.; Huang, Y.; Yan, W. Flotation Behaviors of Perovskite, Titanaugite, and Magnesium Aluminate Spinel Using Octyl Hydroxamic Acid as the Collector. *Minerals* **2017**, *7*, 134. [CrossRef]
17. Welham, N.J.; Malatt, K.A.; Vukcevic, S. The Stability of Iron Phases Presently Used for Disposal from Metallurgical Systems—A Review. *Miner. Eng.* **2000**, *13*, 911–931. [CrossRef]
18. Elwert, T.; Goldmann, D.; Schirmer, T.; Strauss, K.W. Affinity of Rare Earth Elements to Silico-Phosphate Phases in the System Al_2O_3-CaO-MgO-P_2O_5-SiO_2. *Chem. Ing. Tech.* **2014**, *86*, 411. [CrossRef]
19. Konar, B.; Van Ende, M.-A.; Jung, I.-H. Critical Evaluation and Thermodynamic Optimization of the Li_2O-Al_2O_3 and Li_2O-MgO-Al_2O_3 Systems. *Metall. Mater. Trans. B* **2018**, *49*, 2917–2944. [CrossRef]
20. Aoyama, M.; Amano, Y.; Inoue, K.; Honda, S.; Hashimoto, S.; Iwamoto, Y. Synthesis and Characterization of Lithium Aluminate Red Phosphors. *J. Lumin.* **2013**, *135*, 211–215. [CrossRef]
21. Datta, R.K.; Roy, R. Phase Transitions in LiAl5O8. *J. Am. Ceram. Soc.* **1963**, *46*, 388–390. [CrossRef]
22. Konar, B.; Van Ende, M.-A.; Jung, I.-H. Critical Evaluation and Thermodynamic Optimization of the Li-O, and Li_2O-SiO_2 Systems. *J. Eur. Ceram. Soc.* **2017**, *37*, 2189–2207. [CrossRef]
23. Konar, B.; Kim, D.-G.; Jung, I.-H. Critical Thermodynamic Optimization of the Li_2O-Al_2O_3-SiO_2 System and Its Application for the Thermodynamic Analysis of the Glass-Ceramics. *J. Eur. Ceram. Soc.* **2018**, *38*, 3881–3904. [CrossRef]
24. Schirmer, T.; Qiu, H.; Li, H.; Goldmann, D.; Fischlschweiger, M. Li-Distribution in Compounds of the Li_2O-MgO-Al_2O_3-SiO_2-CaO System—A First Survey. *Metals* **2020**, *10*, 1633. [CrossRef]
25. Sartbaeva, A.; Redfern, S.A.T.; Lee, W.T. A Neutron Diffraction and Rietveld Analysis of Cooperative Li Motion in Beta-Eucryptite. *J. Phys. Condens. Matter* **2004**, *16*, 5267–5278. [CrossRef]
26. Perrotta, A.J.; Savage, R.O. Beta Eucryptite Crystalline Solutions Involving P5+. *J. Am. Ceram. Soc.* **1967**, *50*, 112. [CrossRef]
27. Lee, S.-G.; Seo, J.Y.; Lee, J.-W.; Park, W.B.; Sohn, K.-S.; Pyo, M. Composition-Tuned Lithium Aluminosilicate as a New Humidity-Sensing Ceramic Material with High Sensitivity. *Sens. Actuators B Chem.* **2021**, *339*, 129928. [CrossRef]
28. Jin, L.; Wang, J.; Rousselot, S.; Dollé, M.; Chartrand, P. Experimental and Thermodynamic Study of Li-O and Li_2O-P_2O_5 Systems. *Can. J. Chem. Eng.* **2019**, *97*, 2234–2241. [CrossRef]
29. Osterheld, R.K. Liquidus Diagram for the System Lithium Orthophosphate-Lithium Metaphosphate. *J. Inorg. Nucl. Chem.* **1968**, *30*, 3173–3175. [CrossRef]
30. Ayu, N.I.P.; Kartini, E.; Prayogi, L.D.; Faisal, M. Supardi Crystal Structure Analysis of Li3PO4 Powder Prepared by Wet Chemical Reaction and Solid-State Reaction by Using X-Ray Diffraction (XRD). *Ionics* **2016**, *22*, 1051–1057. [CrossRef]
31. Raguž, B.; Wittich, K.; Glaum, R. Two New, Metastable Polymorphs of Lithium Pyrophosphate $Li_4P_2O_7$. *Eur. J. Inorg. Chem.* **2019**, *2019*, 1688–1696. [CrossRef]
32. Murashova, E.V.; Chudinova, N.N. Synthesis and Crystal Structures of Lithium Polyphosphates, $LiPO_3$, Li4H(PO_3)5, and LiMn(PO_3)3. *Crystallogr. Rep.* **2001**, *46*, 942–947. [CrossRef]
33. Kay, H.F.; Bailey, P.C. Structure and Properties of $CaTiO_3$. *Acta Cryst.* **1957**, *10*, 219–226. [CrossRef]
34. Liu, X.; Liebermann, R.C. X-Ray Powder Diffraction Study of $CaTiO_3$ Perovskite at High Temperatures. *Phys. Chem. Miner.* **1993**, *20*, 171–175. [CrossRef]
35. Guyot, F.; Richet, P.; Courtial, P.; Gillet, P. High-Temperature Heat Capacity and Phase Transitions of $CaTiO_3$ Perovskite. *Phys. Chem. Miner.* **1993**, *20*, 141–146. [CrossRef]

36. Wang, Y.; Liebermann, R.C. Electron Microscopy Study of Domain Structure Due to Phase Transitions in Natural Perovskite. *Phys. Chem. Miner.* **1993**, *20*, 147–158. [CrossRef]
37. Vogt, T.; Schmahl, W.W. The High-Temperature Phase Transition in Perovskite. *Europhys. Lett.* **1993**, *24*, 281–285. [CrossRef]
38. Redfern, S.A.T. High-Temperature Structural Phase Transitions in Perovskite. *J. Phys. Condens. Matter* **1996**, *8*, 8267–8275. [CrossRef]
39. Kennedy, B.J.; Howard, C.J.; Chakoumakos, B.C. Phase Transitions in Perovskite at Elevated Temperatures—A Powder Neutron Diffraction Study. *J. Phys. Condens. Matter* **1999**, *11*, 1479–1488. [CrossRef]
40. Ali, R.; Yashima, M. Space Group and Crystal Structure of the Perovskite $CaTiO_3$ from 296 to 1720K. *J. Solid State Chem.* **2005**, *178*, 2867–2872. [CrossRef]
41. Zhang, Z.; Lumpkin, G.R.; Howard, C.J.; Knight, K.S.; Whittle, K.R.; Osaka, K. Structures and Phase Diagram for the System $CaTiO_3$–La2/3TiO_3. *J. Solid State Chem.* **2007**, *180*, 1083–1092. [CrossRef]
42. Cavalcante, L.S.; Marques, V.S.; Sczancoski, J.C.; Escote, M.T.; Joya, M.R.; Varela, J.A.; Santos, M.R.M.C.; Pizani, P.S.; Longo, E. Synthesis, Structural Refinement and Optical Behavior of $CaTiO_3$ Powders: A Comparative Study of Processing in Different Furnaces. *Chem. Eng. J.* **2008**, *143*, 299–307. [CrossRef]
43. Danek, V.; Nerad, I. Phase Diagram and Structure of Melts of the System CaO—TiO_2—SiO_2. *Chem. Pap.* **2002**, *56*, 241–246.
44. De Vries, R.C.; Roy, R.; Osborn, E.F. Phase Equilibria in the System CaO-TiO_2-SiO_2. *J. Am. Ceram. Soc.* **1955**, *38*, 158–171. [CrossRef]
45. Okrusch, M.; Matthes, S. *Mineralogie: Eine Einführung in die Spezielle Mineralogie, Petrologie und Lagerstättenkunde*; Lehrbuch; 9. Aufl; Springer Spektrum: Berlin, Germany, 2014; ISBN 978-3-642-34660-6.
46. Feng, D.; Navrotsky, A. Thermochemistry of Rare Earth Perovskites. *MRS Adv.* **2016**, *1*, 2695–2700. [CrossRef]
47. Chakhmouradian, A.R.; Mitchell, R.H. Three Compositional Varieties of Perovskite from Kimberlites of the Lac de Gras Field (Northwest Territories, Canada). *Mineral. Mag.* **2001**, *65*, 133–148. [CrossRef]
48. Marxreiter, H.; Boysen, H.; Frey, F.; Schulz, H.; Vogt, T. The Structure of the Φ1-Phase CaZr4O9 in Calcium Stabilized Zirconia. *Mater. Res. Bull.* **1990**, *25*, 435–442. [CrossRef]
49. Hellmann, J.R.; Stubican, V.S. The Existence and Stability of Ca6Zr19O44 Compound in the System ZrO_2-CaO. *Mater. Res. Bull.* **1982**, *17*, 459–465. [CrossRef]
50. Yin, Y.; Argent, B.B. Phase Diagrams and Thermodynamics of the Systems ZrO_2-CaO and ZrO_2-MgO. *JPE* **1993**, *14*, 439–450. [CrossRef]
51. Fabrichnaya, O.; Lakiza, S.; Wang, C.; Zinkevich, M.; Aldinger, F. Assessment of Thermodynamic Functions in the ZrO_2–La_2O_3–Al_2O_3 System. *J. Alloy. Compd.* **2008**, *453*, 271–281. [CrossRef]
52. Paul, B.; Singh, K.; Jaroń, T.; Roy, A.; Chowdhury, A. Structural Properties and the Fluorite–Pyrochlore Phase Transition in $La_2Zr_2O_7$: The Role of Oxygen to Induce Local Disordered States. *J. Alloy. Compd.* **2016**, *686*, 130–136. [CrossRef]
53. Ushakov, S.V.; Navrotsky, A.; Weber, R.J.K.; Neuefeind, J.C. Structure and Thermal Expansion of YSZ and $La_2Zr_2O_7$ Above 1500 °C from Neutron Diffraction on Levitated Samples. *J. Am. Ceram. Soc.* **2015**, *98*, 3381–3388. [CrossRef]
54. Tang, Z.; Huang, Z.; Han, W.; Qi, J.; Shi, Y.; Ma, N.; Zhang, Y.; Guo, X.; Lu, T. Uranium-Incorporated Pyrochlore La2(UxMgxZr1–2x)2O7 Nuclear Waste Form: Structure and Phase Stability. *Inorg. Chem.* **2020**, *59*, 9919–9926. [CrossRef] [PubMed]
55. Huang, Z.; Chen, L.; Huang, B.; Xu, B.; Shao, G.; Wang, H.; Li, Y.; Wang, C.-A. Enhanced Performance of $Li_{6.4}La_3Zr_{1.4}Ta_{0.6}O_{12}$ Solid Electrolyte by the Regulation of Grain and Grain Boundary Phases. *ACS Appl. Mater. Interfaces* **2020**, *12*, 56118–56125. [CrossRef]
56. Li, R.; Liao, K.; Zhou, W.; Li, X.; Meng, D.; Cai, R.; Shao, Z. Realizing Fourfold Enhancement in Conductivity of Perovskite $Li_{0.33}La_{0.557}TiO_3$ Electrolyte Membrane via a Sr and Ta Co-Doping Strategy. *J. Membr. Sci.* **2019**, *582*, 194–202. [CrossRef]
57. Li, Y.; Zhang, T.; Feng, Y.; Liu, C.; Jiang, M. Liquid Regions of Lanthanum-Bearing Aluminosilicates. *Materials* **2020**, *13*, 450. [CrossRef]
58. Fukuda, K.; Iwata, T.; Champion, E. Crystal Structure of Lanthanum Oxyorthosilicate, La_2SiO_5. *Powder Diffr.* **2006**, *21*, 300–303. [CrossRef]
59. El Ouenzerfi, R. Investigation of the CaO–La2O_3–SiO_2–P_2O_5 Quaternary Diagram. Synthesis, Existence Domain, and Characterization of Apatitic Phosphosilicates. *Solid State Ion.* **2003**, *156*, 209–222. [CrossRef]
60. Shannon, R.D. Revised Effective Ionic Radii and Systematic Studies of Interatomic Distances in Halides and Chalcogenides. *Acta Crystallogr. Sect. A* **1976**, *32*, 751–767. [CrossRef]
61. Kalsbeek, N.; Larsen, S.; Rønsbo, J.G. Crystal Structures of Rare Earth Elements Rich Apatite Analogues. *Z. Krist. Cryst. Mater.* **1990**, *191*, 249–263. [CrossRef]
62. Kamel, N.; Aït-Amar, H.; Zahri, A. The Use of a Soaking Procedure Combined with the Sintering Process to Reach a High Cerium Content in a Cerium-Bearing Y-Britholite. *Progress Nucl. Energy* **2007**, *49*, 351–364. [CrossRef]
63. Oberti, R.; Ottolini, L.; Della Ventura, G.; Carlo Parodi, G. On the Symmetry and Crystal Chemistry of Britholite: New Structural and Microanalytical Data. *Am. Mineral.* **2001**, *86*, 1066–1075. [CrossRef]
64. Ardhaoui, K.; Coulet, M.V.; Ben Chérifa, A.; Carpena, J.; Rogez, J.; Jemal, M. Standard Enthalpy of Formation of Neodymium Fluorbritholites. *Thermochim. Acta* **2006**, *444*, 190–194. [CrossRef]
65. Lan, X.; Gao, J.; Li, Y.; Guo, Z. Phase Equilibria of CaO–SiO_2–CaF_2–P_2O_5–Ce_2O_3 System and Formation Mechanism of Britholite. *Ceram. Int.* **2021**, *47*, 11966–11972. [CrossRef]

66. Sommerfeld, M.; Vonderstein, C.; Dertmann, C.; Klimko, J.; Oráč, D.; Miškufová, A.; Havlík, T.; Friedrich, B. A Combined Pyro- and Hydrometallurgical Approach to Recycle Pyrolyzed Lithium-Ion Battery Black Mass Part 1: Production of Lithium Concentrates in an Electric Arc Furnace. *Metals* **2020**, *10*, 1069. [CrossRef]
67. Yamauchi, T.; Maruhashi, S. Dephosphorization of Molten Pig Iron Containing Chromium by Lithium Carbonate. *ISIJ Int.* **1983**, *23*, 752–758. [CrossRef]
68. Xue, T.; Wang, L.; Qi, T.; Chu, J.; Qu, J.; Liu, C. Decomposition Kinetics of Titanium Slag in Sodium Hydroxide System. *Hydrometallurgy* **2009**, *95*, 22–27. [CrossRef]
69. Toromanoff, I.; Habashi, F. The Composition of a Titanium Slag from Sorel. *J. Less Common Met.* **1984**, *97*, 317–329. [CrossRef]
70. Wang, M.; Zhang, L.; Zhang, L.; Sui, Z.; Tu, G. Selective Enrichment of TiO_2 and Precipitation Behavior of Perovskite Phase in Titania Bearing Slag. *Trans. Nonferrous Met. Soc. China* **2006**, *16*, 421–425. [CrossRef]
71. Gaballah, I.; Allain, E. Recycling of Strategic Metals from Industrial Slag by a Hydro-and Pyrometallurgical Process. *Resour. Conserv. Recycl.* **1994**, *10*, 75–85. [CrossRef]
72. Li, J.; Guo, Z.; Yang, T.; Yue, Z.; Ma, C. Recovery Behavior of Separating Britholite ($Ca_3Ce_2[(Si,P)O_4]_3F$) Phase from Rare-Earth-Rich Slag by Centrifugal Casting. *High Temp. Mater. Process.* **2014**, *34*, 263–269. [CrossRef]
73. Stefanovsky, S.V.; Stefanovsky, O.I.; Malinina, G.A. Mechanism of Phase Formation in the Batch Mixtures for Slag-Bearing Glass Ceramics—12207. In Proceedings of the WM2012 Conference Proceedings, Phoenix, AZ, USA, 26 February–1 March 2012; pp. 1–8.
74. Terra, O.; Dacheux, N.; Audubert, F.; Podor, R. Immobilization of Tetravalent Actinides in Phosphate Ceramics. *J. Nucl. Mater.* **2006**, *352*, 224–232. [CrossRef]
75. Bale, C.W.; Bélisle, E.; Chartrand, P.; Decterov, S.A.; Eriksson, G.; Hack, K.; Jung, I.-H.; Kang, Y.-B.; Melançon, J.; Pelton, A.D.; et al. FactSage Thermochemical Software and Databases—Recent Developments. *Calphad* **2009**, *33*, 295–311. [CrossRef]
76. Clark, C.M.; Downs, R.T. Using the American Mineralogist Crystal Structure Database in the Classroom. *J. Geosci. Educ.* **2004**, *52*, 76–80. [CrossRef]
77. Lafuente, B.; Downs, R.T.; Yang, H.; Stone, N. 1. The Power of Databases: The RRUFF Project. In *Highlights in Mineralogical Crystallography*; Armbruster, T., Danisi, R.M., Eds.; De Gruyter: Berlin, Germany, 2015; pp. 1–30. ISBN 978-3-11-041704-3.
78. Jercinovic, M.J.; Williams, M.L.; Allaz, J.; Donovan, J.J. Trace Analysis in EPMA. *IOP Conf. Ser. Mater. Sci. Eng.* **2012**, *32*, 012012. [CrossRef]
79. Merlet, C. Quantitative Electron Probe Microanalysis: New Accurate Φ (Pz) Description. In *Electron Microbeam Analysis*; Boekestein, A., Pavićević, M.K., Eds.; Springer Vienna: Vienna, Austria, 1992; Volume 12, pp. 107–115. ISBN 978-3-211-82359-0.
80. Microsoft Corporation. Microsoft Excel. 2018. Available online: https://office.microsoft.com/excel (accessed on 20 February 2022).